UNIVERSITY OF CALIFORNIA, SAN DIEGO

**Randomness in Biological Systems**

A dissertation submitted in partial satisfaction of the
requirements for the degree
Doctor of Philosophy

in

Mechanical Engineering

by

Benjamin Michael Regner

Committee in charge:

Professor Daniel M. Tartakovsky, Chair
Professor Terrence J. Sejnowski, Co-Chair
Professor Jan Kleissl
Professor Ratnesh Lal
Professor Eric Lauga
Dr. Thomas M. Bartol

2014

Copyright
Benjamin Michael Regner, 2014
All rights reserved.

The dissertation of Benjamin Michael Regner is approved, and it is acceptable in quality and form for publication on microfilm and electronically:

_____

_____

_____

_____

_____
Co-Chair

_____
Chair

University of California, San Diego

2014

DEDICATION

To the Deuce

TABLE OF CONTENTS

ACKNOWLEDGEMENTS

The text of this dissertation contains reprints of the following papers, either accepted or submitted for consideration at the time of publication. The dissertation author was the primary investigator and author of these publications.

**Chapter 2**

Regner, B. M., Vučinić, D., Domnisoru, C., Bartol, T. M., Hetzer, M. W., Tartakovsky, D. M., Sejnowski, T. J., "Anomalous diffusion of single particles in cytoplasm", *Biophysical Journal*, 104(8), 1652-1660. 2013.

**Chapter 3**

Regner, B. M., Tartakovsky, D. M., Sejnowski, T. J., (2014). "Identifying Transport Dynamics of Single-Molecule Trajectories", *Biophysical Journal*, *In Review*

## VITA

| | |
|---|---|
| 2006 | B. S. in Engineering Mechanics and Astronautics, University of Wisconsin, Madison |
| 2007-2009 | Graduate Teaching Assistant, University of California, San Diego |
| 2009 | M. S. in Mechanical Engineering, University of California, San Diego |
| 2014 | Ph. D. in Mechanical Engineering, University of California, San Diego |

## PUBLICATIONS

Regner, B. M., Vučinić, D., Domnisoru, C., Bartol, T. M., Hetzer, M. W., Tartakovsky, D. M., Sejnowski, T. J., (2013). "Anomalous diffusion of single particles in cytoplasm". *Biophysical Journal*, 104(8), 1652-1660.

Regner, B. M., Tartakovsky, D. M., Sejnowski, T. J., (2014). "Identifying Transport Dynamics of Single-Molecule Trajectories", *Biophysical Journal*, *In Review*

ABSTRACT OF THE DISSERTATION

**Randomness in Biological Systems**

by

Benjamin Michael Regner

Doctor of Philosophy in Mechanical Engineering

University of California, San Diego, 2014

Professor Daniel M. Tartakovsky, Chair
Professor Terrence J. Sejnowski, Co-Chair

Random fluctuations play a fundamental role in all biological processes, from diffusion-reaction pathways to the stochasticity inherent to genetic variability. Determining how these random processes interact is critical to both understanding and eventually engineering biological systems. This dissertation deals with the dynamics of stochastic transport processes at the cell level. The first chapter presents a description of a novel microscope design to probe diffusive behavior in a cellular extract. The obtained data reveal both superdiffusive and subdiffusive behavior. This chapter also introduces several stochastic processes that capture the observed behavior. Differences in an ergodicity-breaking parameter between the experimental conditions support the use of these models. The second chapter describes a

new algorithm for determining the anomalous scaling exponent of experimental data. The algorithm, which is based on a renormalization group operator, enables one to determine a distribution of anomalous diffusion exponents from single trajectories. When applied to the experimental data from the first chapter, the algorithm identified a rich distribution of anomalous exponents, indicating the nonstationary behavior indicative of transport process transitions. The implications of this result and its future applications are discussed. The third chapter describes a hard-sphere simulation algorithm for modeling reaction-diffusion systems in complex geometry. Details of the implementation and unresolved issues are outlined. The fourth section deals with the problem of derivation of effective transport equations for cellular environments, which are highly crowded and characterized complex geometry. A probabilistic formulation is proposed for solving a closure problem, which determines the effective diffusion coefficient. This chapter concludes with a computational example that serves both to demonstrate the efficacy and robustness of the proposed framework and to outline its possible applications.

# 1 Introduction

## 1.1 Randomness in Biology

When Robert Brown made observations of the eponymous Brownian motion, he initially attributed the erratic movement of pollen grains to an intrinsic "life force". Subsequent observations of non-organic materials, such as mineral aggregates, refuted this theory, but it wasn't until the work of Einstein and Smoluchowski that a molecular basis for the motion was firmly established [55]. Further developments in physics and probability theory continued over the 20th century, providing a solid mathematical foundation for Brownian motion. Importantly, these developments described the behavior of a particle in dilute suspension, where interactions with other particles are minimal. A description of the dynamics of a particle in a complex environment has only recently seen substantial progress, with the application of fractional calculus and modern theories of stochastic processes [85]. Physical systems such as charge transport in amorphous solids [117], diffusion in porous materials [70], and biomolecular diffusion [46] are examples in which the interaction of many particles and complex geometries leads to anomalous dynamics. Due to the ubiquitous nature of anomalous dynamics, it is an active area of experimental and theoretical research [55, 85].

Regarding biophysical processes, due to technical advances in biochemistry, genetics and microscopy, a deluge of data has provided ample opportunities for answering long standing theoretical questions. A particularly intriguing question is how biological machinery, despite working at the molecular scale where all behavior is stochastic, exhibit robust, repeatable dynamics. Examples include the stochastic release of neurotransmitter accomplishing reliable signal transmission [50], random

patterning accurately guiding embryogenesis [35], and stochastic fluctuations reliably driving the metabolic cycle [76]. While in some cases these processes must be stochastic due to their implementation as moleular machines, evolution has developed techniques to increase reliability, but does not utilize them uniformly. For example, muscle innervation is accomplished using electrical gap junctions, where current is directly coupled between cells [5]. However, the majority of connections in the central nervous system are stochastic chemical synapses where cell-to-cell signal transduction has a probability less than one [61]. Macromolecular complexes provide a reaction substrate for many processes, trapping reaction partners in close proximity, such as the G-protein cascade mechanism found at the cell membrane [5]. Yet critical processes, for example the metabolic pathway, proceed by the interaction of freely diffusing molecules in the cytosol, relying on chance encounters to drive reactions forward [76].

An important goal in biophysics is to understand how inherently stochastic processes can produce reliable behavior in living systems. The specific focus of this dissertation is to investigate transport in biological systems, in order to examine how it is expressed in biology and to produce models for understanding and eventually engineering these complicated systems.

## 1.2 Theory of Diffusion

### 1.2.1 Fickian Diffusion

Inspired by the theory of heat conduction, diffusive behavior was first described by Fick [85]. The concentration $C$ of a solute will undergo flux $J$

$$J = -D\frac{\partial C}{\partial x} \tag{1.1}$$

and evolve with time by the transport equation

$$\frac{\partial C}{\partial t} = D\frac{\partial^2 C}{\partial x^2} \tag{1.2}$$

where $D$ is the diffusion coefficient. Fickian diffusion is closely related to Brownian motion, where Fick's equations describe the evolution of an ensemble of particles undergoing Brownian motion. The first description of Brownian motion was

independently derived by Einstein and Smolukowski, who elucidated a linear dependence between the mean-square displacement (MSD) of a particle undergoing Brownian motion and time [38, 134], i.e.

$$\langle X^2 \rangle = Dt. \tag{1.3}$$

The diffusion coefficient $D$ can be calculated using the Stokes-Einstein relation, which relates the drag force of a particle undergoing Stokes' flow to the momentum relaxation time, and can be calculated for a molecule of radius $r$ by

$$D = \frac{RT}{6\pi\mu r N} \tag{1.4}$$

where $R$ is the gas constant, $T$ is absolute temperature, $\mu$ is the dynamic viscosity and $N$ is Avogadro's number. The derivation of (1.3) was early evidence for the atomic nature of matter, and the first method for calculating Avogadro's number. It was subsequently estimated by Perrin with excellent accuracy, $7.15 \times 10^{23}$.[103]

The Brownian motion of a single particle was first described by Langevin using the equation bearing his name

$$m\frac{d^2\mathbf{x}}{dt} = -\lambda\frac{d\mathbf{x}}{dt} + \eta(t) \tag{1.5}$$

where $m$ is the mass of the particle, $\lambda$ is the hydrodynamic friction and $\eta$ is a time-varying stochastic forcing due to random collisions with solvent molecules. An alternative description is the Fokker-Planck equation where Brownian motion with drift is given by

$$\frac{\partial p(x,t)}{\partial t} = -\frac{\partial}{\partial x}\left[A(x,t)p(x,t)\right] + \frac{1}{2}\frac{\partial^2}{\partial x^2}\left[B(x,t)p(x,t)\right] \tag{1.6}$$

where $p(x,t)$ is a normalized concentration, or probability distribution, $A$ is a drift coefficient and $B$ is a diffusion coefficient [43]. This can be written equivalently in the form of a stochastic differential equation

$$dX_t = A(X_t,t)dt + \sqrt{B(X_t,t)}dW_t \tag{1.7}$$

where $W_t$ is the Wiener process. The Wiener process plays a critical role in the theory of stochastic processes, and is used extensively in the construction of more sophisticated processes [96].

### 1.2.2 Anomalous Diffusion

Further development of diffusion theory was driven by experimental observations of anomalous diffusion, in which the MSD has a power law dependence with time, i.e.

$$\langle X^2 \rangle = Dt^{\alpha} \tag{1.8}$$

where $\alpha$ is the anomalous diffusion coefficient. $\alpha < 1$ is called subdiffusive, and $\alpha > 1$ superdiffusive behavior. Recently, an analysis of mean-square displacment proved that anomalous diffusion can arise from three possible sources. A random walk, or more generally a stochastic process, will generate anomalous dynamics if the increments of the process are not independent, the increments are not wide-sense stationary or the process has non-zero drift [99]. Furthermore, it was shown in the same work that a linear relation between MSD and time is not a sufficient condition to determine if a process is Brownian. Providing a more complete alternative to MSD, a renormalization group operator was proposed to classify the anomalous scaling exponent of stochastic processes. The stochastic process $X(t)$ is called the fixed point of the operator $R_{p,r}$ if

$$X(t) \stackrel{d}{=} R_{p,r}X(t) \equiv \frac{X(rt)}{r^p} \tag{1.9}$$

where $\stackrel{d}{=}$ means equal in probability distribution [98]. The anomalous diffusion coefficient is related by $\alpha = 2p$, and a process with scaling $p$ is said to be p-diffusive. This definition can be rewritten to evoke the Hausdorff dimension, drawing parallels to known descriptions of self-similar behavior [99].

In Chapter 3, we use this framework to develop an algorithm for determining the anomalous diffusion exponent from experimental data. The algorithm determines a distribution of the anomalous scaling for a single realization of a stochastic process. The mean of the distribution is equivalent to the anomalous diffusion exponent, while the distribution gives a sense of the local behavior observed in the realization. We analyze experimental data to show how MSD can give an misleading picture of the observed dynamics. Finally, using a moving window, a realization can be classified over time to provide local information about scaling

of the process. We propose using this method to extract functional information from biological systems.

A variety of dynamical processes that generate anomalous diffusion have been proposed. A classic process that generates anomalous diffusion is fractional Brownian motion (fBM) [80]. Fractional Brownian motion is a random walk with a two-point correlation function given by

$$\langle x(t_1)x(t_2)\rangle = K_H(t_1^{2H} + t_2^{2H} - |t_1 - t_2|^{2H}) \tag{1.10}$$

where $K_H$ is a fractional diffusion constant and $H = \alpha/2$ is the Hurst exponent. Statistics resembling fractional Brownian motion have been observed in diffusion processes in biological systems [60, 40].

Continuous time random walks (CTRW) have been used successfully in describing a variety of anomalous dynamics [89, 117, 15]. CTRW can be described by a generalized master equation (GME)

$$\frac{\partial p(\mathbf{s},t)}{\partial t} = -\sum_{\mathbf{s}'}\int_0^t \phi(\mathbf{s}'-\mathbf{s},t'-t)p(\mathbf{s},t')dt' + \sum_{\mathbf{s}'}\int_0^t \phi(\mathbf{s}-\mathbf{s}',t-t')p(\mathbf{s}',t')dt' \tag{1.11}$$

where $p(\mathbf{s},t)$ is normalized concentration, and $\phi(\mathbf{s},t)$ is a kernel describing the spatial and temporal dynamics of the system in question. A more intuitive description is to consider a standard random walk in which the spatial increments are distributed, such as Brownian motion where they are Gaussian distributed. In a CTRW framework, the time between steps is also distributed, often following a long-tailed power law distribution when studying anomalous dynamics [15]. Results from biological diffusion experiments have been described using CTRW statistics [59, 51].

The equivalence between CTRW and a GME also implies the equivalence between CTRW and a fractional Fokker-Planck equation (FFPE). The development of descriptions using fractional dynamics has recently seen rapid progress, exposing a rich mathematical landscape beyond the scope of this thesis [86]. The FFPE can be derived from the CTRW framework [11], and is given by

$$\frac{\partial p}{\partial t} = {}_0D_t^{1-\alpha}\left[\frac{\partial}{\partial x}\frac{V'(x)}{m\eta_\alpha} + K_\alpha\frac{\partial^2}{\partial x^2}\right]p(x,t) \tag{1.12}$$

where ${}_0D_t^{1-\alpha}$ is the Riemann-Liouville operator. Similarly, a fractional diffusion equation (FDE) has been derived [85]. The form most similar to the classic diffusion equation is

$$\frac{\partial p}{\partial t} = {}_0D_t^{1-\alpha} K_\alpha \frac{\partial^2}{\partial x^2} p(x,t) \tag{1.13}$$

where $K_\alpha$ is an anomalous diffusion exponent. Recent work has proven equivalence between CTRW, FFPE and FDE [85], and exploration of the mathematical properties and applications to data remain an active field of research.

## 1.3 Light Microscopy

Although diffusion can be observed at the macroscale, such as milk gently introduced to coffee, fundamentally the dynamics occur at the molecular level. In biological systems, observing diffusing molecules is complicated by a number of factors, including encasement by cell membranes, high concentrations of biomass, and the typically small size of interesting biomolecules. Furthermore, diffusion is a dynamical process, occuring in sensitive living entities that require percise conditions for normal function. Electron microscopy allows visualization at these small scales, but requires fixation, either chemical or cryogenic, arresting diffusion and the living processes of interest [139]. Due to these complications, descriptions of diffusion in biological systems has been slow and a number of open questions remain. However, recent advances in light microscopy have provided a wealth of data and drawn increased interest in understanding diffusion processes in biology.

### 1.3.1 Light Microscopy

The simplest light microscope uses bright field illumination, where an entire sample is illuminated from the back, and images are captured on the retina using an eyepiece, photographic film, or a CCD camera for digitalization [91]. Biological samples typically have low contrast, making it difficult to resolve details, although contrast agents such as dyes can help. Furthermore, the resolution of bright field illumination is poor. While this technique is still used for a variety of experiments, it is not well suited for probing diffusive behavior.

Fluorescent microscopy is the most commonly used light microscopy technique in use today [91]. Molecules of interest can be tagged, through chemical or genetic means, with a fluorophore molecule that is excited by incident light. The fluorophore is excited into a higher energy state, before rapidly decaying, emitting a photon. A fluorophore will have a specific excitation and emission spectrum that is a function of their structure. Fluorophores commonly used in microscopy have a large shift between their excitation and emission spectra, called the Stokes shift. This shift is exploited in the epifluoroescent microscope, in which the excitation light and the emission light traverse the same optical path. Because the excitation and emission spectra are different, dichroic mirrors and optical filters can be used to ensure only the photons emitted by the molecules of interest are collected on the imaging device [91].

A common imaging modality is video microscopy, in which the entire sample is illuminated using a lamp and the emitted photons are collected on a CCD camera. An alternative design is to raster scan a laser across the sample using galvanized mirrors, collecting emitted photons with a photomultiplier, and obtaining a photon count for each specific location in space. A 2D image is then reconstructed, pixel by pixel, using these photon counts. In order to obtain 3D data, the focal plane must be shifted, typically using a motorized stage. An improvement on this basic scheme is confocal methods, which improves resolution by removing out-of-plane photons [29]. Another improvement is multiphoton excitation, in which two lower energy photons simultaneously excite a fluorophore. Advantages of two-photon microscopy is improved tissue penetration due to lower scattering of low energy photons, reduced photodamage, and improved resolution in the z dimension due to a narrower point spread function [34].

A main issue for resolving biomolecules of interest is the diffraction limit, first recognized by Abbe [1]. The diffraction limit determines the limit of separation between two point sources at which the point spread functions are indistinguishable [91]. Recent work has shown that improvements can be made to the classically assumed limit [105], but it is not possible to completely overcome this limit. However, a single particle can be localized to the nanometer accuracy by

fitting a Gaussian to the point spread function, so that high spatial resolution can be obtained if single particles can be isolated.

One method for superresolution imaging is the probabilistic photoactivation of small numbers of molecules, such that only a few are fluorescing during a given imaging sequence, decreasing the probability that the currently illuminated molecules overlap. Two methods using this idea were recently developed in parallel, photo activated localization microscopy (PALM) [17] and stochastic optical reconstruction microscopy (STORM) [109]. Further refinements have been made to these methods, but in general they suffer from poor temporal resolution. Another superresolution method involves shaping the excitation area by depleting the surrounding area, referred to as stimulated emission depletion microscopy (STED) [52]. Although excellent localization is achieved using this modality, the method is difficult to implement, and again the temporal resolution for large fields of view is poor.

Techniques for capturing data in 3D have also seen recent advances. Light sheet microscopy structures the excitation beam into a thin plane of light that can be rapidly scanned across the sample [62]. While this method has good temporal resolution, the spatial resolution is limited. Several techniques have been proposed that rely on postprocessing of the images to accurately obtain the location. In structured illumination microscopy, spatial modulation of the excitation beam is introduced using a fine grating. The resulting images are analyzed using frequency analysis to recover the fluorophore positions [48]. Another method of improving spatial resolution is by engineering the point spread function of the excited fluorophores. A recently proposed method uses a double helix point spread function and post processing to obtain accurate positions of molecules in 3D [102]. These techniques are undergoing rapid development and improvement, and will continue to be a critically important field of research to probe new experimental questions.

In Chapter 2, we discuss an epifluorescent microscope design in which the galvanized mirrors and stage are replaced by acousto-optic deflectors. The design allows rapid acquisition of 3D volumes with no moving parts [135]. We use this microscope to explore 3D anomalous diffusion in a cellular extract taken from

*Xenopus* oocytes. By tracking polymer microspheres, we observe superdiffusive transport along microtubules with an anomalous exponent of $\alpha = 1.5$. We then apply nocodazole, a chemical known to depolymerize microtubules, and observe subdiffusive transport with $\alpha = 0.6$. We propose the use of fractional Brownian motion to model microtubule transport, and a CTRW to model the subdiffusive transport in the cytosolic fraction. Finally, we validate the use of these models by comparing distributions of an ergodicity-breaking parameter for experimental and simulated data.

### 1.3.2 Analysis Techniques

Given the microscopy methods described above, there are several ways in which they can be used for probing diffusive behavior. A common method for diffusion analysis is fluorescence correlation spectroscopy (FCS). In this method, correlations in the fluctuations of fluorescence intensity are used to derive diffusion dynamics. This is accomplished by looking at fluctuations in a very small volume, where the entrance and exit of individual molecules produces significant changes in the intensity. By measuring the correlations in these fluctuations and applying an appropriate model, the average concentration and diffusion coefficient can be derived [127].

An alternative similar to FCS is fluorescence recovery after photobleaching (FRAP). In this modality, a focal spot is intensely irradiated by the excitation laser to photobleach the fluorophores present in that location. Photobleaching occurs when a fluorophore is overexposed and loses the capability to fluoresce. The photobleached spot is then imaged over time as unbleached molecules diffuse into the dark area. The rate at which the intensity in the area increases can be used to derive the diffusion coefficient [8].

The most straightforward method is to track the trajectory of an individual particle, or single particle tracking (SPT). However, a variety of problems arise in video analysis, including localization in high particle densities, heterogeneity of particle motion, the disappearance of particles due to blinking or moving out of the focal plane and the apparent merging and splitting of particles as they diffuse

past each other [57]. Although superresolution techniques have been designed to overcome some of these problems, they often have poor temporal resolution, precluding analysis of small particles with rapid diffusion. Despite these problems, it is the gold standard for diffusion studies due to the unparalleled detail it provides.

## 1.4 Anomalous Transport in Biological Systems

Characterizing and distinguishing transport mechanisms within a biological cell is critical to understanding cellular function. Stochastic transport processes, such as diffusion, active transport, and cytoskeletal transport, perform the majority of signal transduction within the cell. These processes can be characterized by the mean-square displacement (1.8), with the two parameters of interest being the diffusion coefficient $D$ and the anomalous diffusion exponent $\alpha$. The molecular diffusion coefficient can be calculated using (1.4), but in the presence of crowding the effective diffusion coefficient may be smaller. This has been observed in a variety of biological contexts [55]. Conditions in which anomalous diffusion is observed, where $\alpha \neq 1$, remains relatively underexplored. An excellent review by Höfling and Franosch compiles much of the literature on intracellular and membrane transport [55]. Below is a short overview of the available literature, with specific focus on intracellular transport.

In biological systems, molecules are present at high concentrations, with estimates putting macromolecular volume fraction between 20-30% [39]. Electron microscopy studies reveal how large macromolecular complexes, organelles, and cytoskeletal components combine to produce a dense environment that interacting biomolecules must navigate [83]. For small molecules, the result is to lessen the effective diffusion coefficient, while the dynamics remain well described by Fickian diffusion [32]. However, it is thought that as the volume fraction $\phi = V_{molecule}/V_{total}$ approaches the percolation threshold, anomalous diffusion begins to dominate [114]. The conditions in which anomalous diffusion is observed at this scale, and whether experimental observations have been real or an artifact, remain controversial [37]. However, there is sufficient evidence to suspect that

more sophisticated treatments will improve our understanding of these systems. Furthermore, high volume fraction changes the effective concentration for a given molecule by decreasing the available volume, significantly impacting non-specific interactions and macromolecular association rates [88, 141]. Obtaining accurate reaction rates *in vivo* remains a problem, further complicating questions about the role molecular interactions play in observations of anomalous diffusion [49].

Early studies of biological diffusion focused on the cell membrane, due to the ease of microscope access. Experimental investigation of the membrane led to observations of diverse transport modalities, including Brownian motion, directed motion, confined motion and anomalous diffusion [115]. An important finding is that diffusion can show transient anomalous behavior at short times and Brownian motion at long times, although interpretation of this result can be complicated [113]. Another important class of motion is confined motion, in which a particle appears to undergo Brownian motion, but is trapped in a subdomain [75]. Finally, directed motion, in which a molecule appears to move at constant velocity, has been oberved in the cell membrane [115]. Compared to the intracellular space, the cell membrane has received significant attention. An important goal is to understand if and how these transport processes manifest in the intracellular space [114].

At present, there are few studies that have shown anomalous diffusion in living cells. Caspi et al. introduced microspheres into a cell and observed superdiffusive transport along the cytoskeleton with $\alpha \approx 1.5$ [25, 26]. Seisenberger et al. observed single viruses infecting a cell and analyzed their diffusive motion. They found that the virus underwent subdiffusive transport in the cytoplasm ($0.5 < \alpha < 0.9$) and in the nuceleus ($0.6 < \alpha < 0.9$). Furthermore, they observed directed transport, which they modeled using Brownian motion with drift [119]. Tolic-Norrelykke et al. tracked lipid granules inside yeast cells and observed subdiffusive behavior in the cytoplasm ($\alpha \approx 0.7$) [128]. Golding et al. tracked the diffusion of mRNA within *E. Coli* and observed subdiffusive scaling in the cytoplasm ($\alpha \approx 0.7$) [46]. Bronstein et al. observed the diffusion of telomeres in the nucleus of eukaryote cells and found subdiffusive behavior ($\alpha \approx 0.3$) [20]. Niu and

Yu used a photo activatable version of a cytoskeletal protein FtsZ to obtain intracellular diffusion trajectories, finding one population that was roughly stationary and another population undergoing anomalous subdiffusion ($\alpha \approx 0.7$) [95].

In order to broadly consider the effects of molecule size and concentration on anomalous diffusion, Banks and Fradin used FCS to measure diffusion curves of a variety of tracer proteins of different sizes in a solution crowded by dextran molecules of varying size. They produced effective diffusion coefficient and anomalous exponent curves at different concentrations for many combinations of tracer and dextran molecules, and found that the anomalous diffusion exponent decreases with increasing crowding concentration [9]. A similar study was conducted by Sanabria et al., who found anomalous diffusion for various biomolecules in silica nanostructures [112].

## 1.5 Modeling Diffusion Processes

In Chapter 4, we use a probabilistic formulation to obtain the effective diffusion coefficient in a reconstruction of brain tissue. Homogenization and upscaling of the pore-scale diffusion equation leads to the definition of an effective diffusion coefficient for a unit cell. In the case of purely diffusive flow, the diffusion coefficient is calculated by the solution of a Neumann problem. We use Monte Carlo simulations of a reflecting Brownian motion to obtain a solution to the Neumann problem [21], where the boundary conditions are specified by the upscaling procedure. We apply this method to a surface mesh reconstruction of rat neural tissue, in hippocampal CA1, to obtain an effective diffusion coefficient.

In Chapter 5, we discuss efforts to implement volume-filling hard sphere molecules in the MCell simulation environment. MCell is a Monte Carlo simulator of diffusion-reaction equations in complex surface geometries. In the current version, all molecules are represented as point particles. In order to begin to investigate the effects of crowding in real tissue, we began an implementation of hard sphere molecules using the Bullet physics engine. MCell solves the ray tracing problem of a reflecting Brownian motion in a complex geometry with surface reac-

tions. The intent was to replace the ray tracing algorithms in MCell with the Bullet implementation in which objects can be any shape. However, it was realized mid-development that the dynamics of hard sphere simulations require simultaneous time stepping of all molecules, instead of the queue-based time stepping allowed with point particles. Impending changes to the code base will make implementing simultaneous time stepping significantly easier.

# 2 Anomalous Diffusion of Single Particles in Cytoplasm

## 2.1 Introduction

Diffusion plays a fundamental role in every biochemical process in living cells. Just as essential for intracellular transport is cytoskeletal migration, which includes all motor protein-mediated transport. Characterizing and distinguishing these and other transport mechanisms within a cell is critical to understanding cellular function. Topologic complexity of crowded intracellular space renders mathematical representations of processes as basic as molecular diffusion problematic. While some studies [28, 66] relied on Brownian motion to represent intracellular diffusion, others [88, 132] found evidence of anomalous (non-Fickian) diffusive behavior that requires the use of more evolved random walk models (e.g., fractional Brownian motion and continuous time random walk described below).

Modeling cytoskeletal transport is even more challenging, since it involves a complex interplay of various mechanisms. These include the variety of molecular motors that traverse the cytoskeleton [131, 72], cytoskeleton self-assembly kinetics [65, 45], and the interaction between microtubule and actin filament transport [121, 22]. Many of these processes are fundamentally different from Fickian diffusion, and initial work has successfully modeled cytoskeletal transport as anomalous diffusion [25, 26]. A major goal of our analysis is to extend this knowledge by elucidating the underlying processes from single-particle measurements and to identify useful modeling tools for future efforts.

An immediate impetus for studying intracellular transport comes from elec-

tron microscopy studies, which revealed how large macromolecular complexes, organelles, and cytoskeletal components combine to produce a dense environment that interacting biomolecules must navigate, either through diffusion or cytoskeletal transport [83]. However, the fixation required for electron microscopy arrests diffusive motion making light microscopy critical for characterizing these processes. Recent advances in light microscopy gave rise to a number of experiments looking at intracellular transport [9, 20, 119, 25, 128, 46]. The three-dimensional (3D) single-particle tracking experiments reported below will add to the growing understanding of diffusion and other transport mechanisms in biological systems.

### 2.1.1 Experiment Description

We consider three distinct, biologically relevant conditions to acquire particle trajectories. Specifically, single fluorescent microspheres are tracked in a buffer solution, a cellular extract with microtubules intact, and an extract with depolymerized microtubules. The use of an extract, prepared from *Xenopus* eggs (rather than from intact live cells) greatly simplifies the experiments, while maintaining an environment statistically similar to the in vivo intracellular space. The protein concentration in the cytosolic fraction was approximately 100 mg/ml, similar to protein concentrations seen in live cells.

Single-particle tracking is a powerful technique that has become common in analyzing diffusion in biological systems [59]. However, particle tracking methods are typically limited to two dimensions due to the physical constraints on the speed of moving the sample or the microscope objective in the third dimension. We developed a light microscopy technique that employs acousto-optic deflectors (AODs) to realize 3D imaging of volumes with high temporal resolution and no macroscopically moving parts [135, 23]. Several recent AOD microscopes employed a 4-AOD setup to produce 3D random access, two-photon imaging in tissue; these devices use point scanning to increase temporal resolution [47, 68, 110]. Point scanning is inappropriate for tracking single molecules, because the stochastic nature of their movements requires rapid scanning of the entire volume within which the particle is moving. Our microscope employs a simpler 2-AOD setup to perform rapid raster

scans of small volumes, which enabled us to record single-particle trajectories.

### 2.1.2 Fickian and non-Fickian Diffusion

Single-particle tracking microscopy enables one to track how the position $\mathbf{X}_i(t)$ of the $i$-th fluorescent microsphere changes with time $t$. These trajectories can be used to compute the mean-square displacement (MSD) over $N$ microspheres,

$$\langle \delta^2(t) \rangle = \frac{1}{N} \sum_{i=1}^{N} \|\mathbf{X}_i(t) - \mathbf{X}_i(0)\|^2 \tag{2.1}$$

where $\langle \cdot \rangle$ denotes the ensemble average. The MSD characteristic of Fickian diffusion grows linearly with time,

$$\langle \delta^2 \rangle = 6 D_\alpha t \tag{2.2}$$

where $D_\alpha$ is a diffusion coefficient. For diffusion in free space (solvent fluid), $D_\alpha$ can be calculated from the Stokes-Einstein relation

$$D_\alpha = \frac{k_B T}{6 \pi \mu r} \tag{2.3}$$

where $k_B$ is the Boltzmann constant, $T$ is temperature, $\mu$ is the viscosity of the solvent fluid, and $r$ is the radius of the diffusing molecule. If Fickian diffusion takes place in a crowded environment whose pores are filled with a solvent fluid, the value of $D_\alpha$ is reduced to account for the medium's porosity and tortuosity. Such a reduction in "effective" diffusion coefficient $D_\alpha$ has been observed in a variety biological phenomena [9, 90, 78].

Diffusion processes in which the MSD grows nonlinearly with time,

$$\langle \delta^2 \rangle = 6 D_\alpha t^\alpha, \tag{2.4}$$

are referred to as anomalous or non-Fickian. A process is called sub-diffusion if $0 < \alpha < 1$, and super-diffusion if $1 < \alpha < 2$; $\alpha = 1$ corresponds to Fickian (classical) diffusion, and $\alpha = 2$ is known as the ballistic limit [86]. Anomalous diffusion has been observed at a variety of scales in a plethora of applications, including solute transport in geologic formations [16, 92], transport of polynucleotides through pores [84, 12], and diffusion of fluid through tissue [73, 97]. Anomalous diffusion

has also been observed in cytoskeletal transport [25, 26], and a main goal of this report is to identify transport mechanisms that could give rise to this behavior.

A time-averaged MSD provides a useful alternative to the ensemble-averaged MSD, especially in biological systems in which it is common to have only a few trajectories with a relatively short observation time. The time-averaged MSD of the $i$-th microsphere is defined by

$$\overline{\delta_i^2}(\Delta, t) = \frac{1}{t-\Delta}\int_0^{t-\Delta} [\mathbf{X}(t'+\Delta) - \mathbf{X}(t')]^2 \mathrm{d}t' \tag{2.5}$$

where $\Delta$ is a lag time [104]. The ensemble average of the time-averaged MSDs for all $N$ experimental trajectories, $\langle\overline{\delta^2}\rangle = (1/N)\sum_{i=1}^{N}\overline{\delta_i^2}$, is then fit with an equation

$$\langle\overline{\delta^2}\rangle = 6D_\alpha\Delta^\alpha + C. \tag{2.6}$$

The fitting parameter $C$ accounts for noise in the measurements of trajectories, such that a noiseless MSD would be fit with $C = 0$. In the following analysis the experimental MSD is shifted by subtracting this constant, which can be thought of as removing noise. Analysis without this shift gave qualitatively similar but quantitatively inferior results. Despite a long history of using the ensemble-averaged MSD for analyzing random walks [59], recent work has shown that it can produce misleading results [77, 129]. Furthermore, many single-particle tracking experiments in biology have shown that comparing the time-average MSD for different particles does not necessarily match the ensemble-averaged MSD [10].

Stochastic processes whose time-averaged behavior differs from its ensemble (over multiple realizations) average are called non-ergodic [44]. Ergodicity or lack thereof is an intrinsic property of a process. Experimental verification of a process' ergodicity requires observation times that are sufficiently long for the process to self-average. The practical limits on observation time imposed by our microscope do not provide sufficient time for a given trajectory to self-average, making ergodicity analysis inappropriate. Instead, we analyze a pre-ergodic regime in which robust non-ergodic measures can be observed [59]. We define the dimensionless ratio $\xi_i = \overline{\delta_i^2}/\langle\delta^2\rangle$, and obtain a distribution $\phi(\xi_i)$ of time-averaged MSDs. This distribution can be used to characterize the ergodic properties of the process, such

that $\phi(\xi) = \delta(\xi - 1)$, where $\delta$ is the Dirac delta function, denotes an ergodic process, and divergence from this distribution reveals ergodicity breaking.

### 2.1.3 Random Walk Models of Anomalous Diffusion

In "classical" random walk models, the final position $X_N$ of a particle after $N$ equal time steps is a sum of $N$ random spatial increments $\Delta x_n$ $(n = 1, \ldots, N)$,

$$X_N = \sum_{n=1}^{N} \Delta x_n. \tag{2.7}$$

The choice of a probability density function (PDF) for these increments, $\psi_{\Delta x}(\cdot)$, uniquely specifies a model of this class. For example, a Gaussian PDF $\psi_{\Delta x}(\cdot)$ corresponds to Brownian motion (BM).

The continuous time random walk (CTRW) generalizes this classical framework by allowing for time increments, $\Delta t_n$ $(n = 1, \ldots, N)$, of variable (and random) duration. Thus, CTRW is characterized by two PDFs: one for random time increments, $\psi_{\Delta x}(\cdot)$, and the other for random time increments, $\psi_{\Delta t}(\cdot)$. After $N$ steps of the CTRW, it takes a particle the time

$$T_N = \sum_{n=1}^{N} \Delta t_n \tag{2.8}$$

to reach its position $X_n$ given by Eq. 2.7. The choice of the PDFs $\psi_{\Delta x}(\cdot)$ and $\psi_{\Delta t}(\cdot)$ defines a manifold in the space of CTRW models. For example, selecting $\psi_{\Delta x}(\cdot)$ to be a power law and requiring $\psi_{\Delta t}(\cdot)$ to have a finite mean value yields a family of Lévy flight models. The latter were used to describe a wide range of seemingly random phenomena, such as search patterns of flying albatrosses [133], human travel [19], and financial markets [81]. Another combination of these two PDFs, a Gaussian $\psi_{\Delta x}(\cdot)$ and a power-law $\psi_{\Delta t}(\cdot)$, results in a particle's MSD that exhibits sub-diffusive scaling with time [116, 85] and was used to model sub-diffusive transport in biological systems [60, 10]. In this regime, a particle's MSD exhibits weak ergodicity breaking and the mean value of random time increments $\Delta t_n$ does not exist [51]. This renders the calculation of a time-averaged MSD problematic and necessitates the reliance on an analytically derived distribution of

time-averaged MSDs [51],

$$\lim_{t\to\infty} \phi_\alpha(\xi) = \frac{\Gamma^{1/\alpha}(1+\alpha)}{\alpha\xi^{1+1/\alpha}} l_\alpha \left[\frac{\Gamma^{1/\alpha}(1+\alpha)}{\xi^{1/\alpha}}\right]. \tag{2.9}$$

Here $\alpha$ comes from the underlying temporal distribution used in the derivation, $\psi_{\Delta t}(\cdot) \sim \Delta t^{-(1+\alpha)}$, $\Gamma(x)$ is the gamma function, and $l_\alpha(x)$ is the one-sided Lévy stable distribution. Using this analytical distribution, the pre-ergodic analysis performed on the experimental data can be directly compared to a CTRW model.

Fractional Brownian motion (fBM) is another generalization of the classical random walk, which postulates that taking a step in one direction changes (increases or decreases, depending on the correlation) the probability that the next step will be in the same direction [56]. This non-Markovian process is characterized by a two-point correlation function

$$\langle x(t_1)x(t_2)\rangle = K_H(t_1^{2H} + t_2^{2H} - |t_1 - t_2|^{2H}) \tag{2.10}$$

where $K_H$ is a fractional diffusion constant and $H = \alpha/2$ is the Hurst exponent. The fBM framework was used to model intracellular diffusion [40]. It has been shown recently that fBM is ergodic in the limit of large observation times, although for short observation times this is not the case [59].

We use measurements of single-particle trajectories in cytoplasm to discriminate between these three alternative random-walk interpretations, i.e., to select a model that captures best both molecular diffusion in crowded environments and cytoskeletal transport along microtubules. To achieve a robust model selection, we rely on the fact that BM, CTRW, and fBM have distinct ergodic behaviors, particularly when observation time is short [59]. This makes pre-ergodic analyses uniquely suited for single-particle tracking in biological systems that are often characterized by strict limits on observation time. We show that a pre-ergodic analysis can be leveraged to differentiate each experimental condition and to identify a corresponding random walk model.

## 2.2 Methods

### 2.2.1 Xenopus Egg Extract Preparation

*Xenopus* egg extract is prepared using the protocol described by Hetzer et al. [53]. Only the cytosolic fraction described is used in this study.

### 2.2.2 Microsphere Preparation and Imaging

Streptavidin coated fluorescent microspheres from Polysciences (Warrington, PA) are prepared as specified by manufacturer instructions, resuspended in PBS/BSA binding buffer (0.02 M phosphate buffer, 8 mg/ml NaCL, 10 mg/ml BSA) at a concentration of 1.25% and stored at 4° C. The microspheres have a diameter of 1.019 $\mu$m ($\pm$0.018 $\mu$m), excitation frequency peak at 441 nm and emission peak at 486 nm. These are introduced into extract at a concentration determined by experiment where a concentration is chosen based on sparse but plentiful microsphere coverage when viewed by microscope, allowing easy acquisition of long trajectories without capturing trajectories where some frames have overlapping microspheres. This resulting solution is deposited onto uncoated glass slides, covered with a coverslip, and sealed using nail polish to minimize evaporation. The sample thickness is estimated to be roughly 10 $\mu$m. This is determined by focusing on microspheres stuck to the slide, and measuring the distance traveled by the stage to put the microspheres stuck to the coverslip in focus. As the extract contains microtubules, there is also a question as to how they are ordered. Although this is difficult to determine with our setup, it is expected that the microtubules will be randomly distributed and unordered, although it may be there is some bias toward the plane of the slide, as the sample volume is comparatively narrow in the orthogonal direction. For the case of the buffer solution, the microspheres are diluted in PBS to again obtain a sparse coverage. To remove cytoskeletal transport along microtubules and investigate free diffusion in the cytosolic fraction, nocodazole is applied, which is known to interfere with microtubule polymerization. The extract is incubated at 37° C for 1 hour with 10 $\mu$M nocodazole, similar to previous protocols [25]. The resulting solution is again deposited onto coverslips with sparse

coverage.

### 2.2.3 Acousto-optic Deflector Microscopy

In this study we use a microscope that uses acousto-optic deflectors (AODs) to guide a laser beam instead of mirrors [135]. A block diagram of this microscope can be found in Fig. 2.1 *A*. An AOD is a device that introduces sound waves into a transparent crystal to form a transient diffraction grating. The angle of optical diffraction is related to the frequency of sound so that the available range of beam deflection is given by the equation

$$\Delta\theta \approx \frac{\lambda \Delta f}{v} \tag{2.11}$$

where $\Delta\theta$ is the total sweep angle, $\lambda$ is the optical wavelength, $\Delta f$ the acousto-optic bandwidth, and $v$ the speed of sound in the acoustic medium. It is apparent from this equation that sweeping the acoustic frequency through a given range will direct the focus along a line. The use of two orthogonal AOD's therefore produces raster scanning in the $(x, y)$ plane [23]. A cylindrical lensing effect is created by the finite propagation time of the sound wave, so that the effective focal length $(F.L.)$ of an AOD sweeping through a range of acoustic frequencies is given by

$$F.L. = \frac{v^2}{\lambda}\left(\frac{\mathrm{d}f}{\mathrm{d}t}\right)^{-1}, \tag{2.12}$$

where $\mathrm{d}f/\mathrm{d}t$ is the rate of change of the sound frequency. By prescribing a precise range of frequencies and several rates of sweeping, one for every desired focal plane, a full 3D volume can be imaged at a rate on the order of 100 Hz [23].

Our setup uses an integrated 2D acousto-optic deflector from Brimrose (Sparks, Maryland), model 2DS-100-45-100, which consists of two orthogonally mounted TeO2 AODs. This device is placed in line with a collimated 405 nm single mode laser diode. A 1:1 telescope directs the beam onto the back aperture of a 40× oil immersion objective with 1.35 NA. The refractive index of the oil used for all slides imaged is 1.518. Emitted light is collected by a Hamamatsu (Bridgewater, NJ) H7422-40 photomultiplier tube and acquired by a LeCroy (Chestnut Ridge, NY) WaveRunner 64Xi oscilloscope. The AODs are driven by an Analog Devices

(Norwood, MA) AD9959 direct digital synthesizer (DDS), which is controlled by custom firmware on an Altera (San Jose, CA) Cyclone 2 field-programmable gate array (FPGA). The FPGA circuit is designed and implemented in-house and provides tight control over the timing of the scan. Further details can be found in Appendix A. All acquired images are saved in the NetCDF scientific data format [107] which preserves the intensity of each pixel and allows labeling with metadata for parameters such as voxel size in physical units. Conversion to common graphical formats for post-processing and analysis is provided by an in-house ImageJ plugin [2]. This setup results in a maximum field of view of approximately $102 \times 102$ $\mu$m$^2$, and a varying focal length up to 20 $\mu$m from the fixed nominal focal plane of the objective.

In previous work using AODs it was noted that a 2-AOD scanner necessarily produces astigmatic 3D scans [110]. This is incorrect. A simple solution for the astigmatism is to scan at an angle to the 2-AOD system's acoustic propagation axes. If both AOD channels are sweeping the sound frequencies at the same rate, this results in a raster scan oriented at 45 degrees to the AOD devices' orientations with the effective focal lengths of both AODs being equal, i.e., without astigmatism. If the two AODs are simply mounted behind one another without a 1:1 telescope between them as in our simple system, the effective focal planes will not be parfocal; in such a setup the astigmatism is fully corrected by tilting the scan direction at an angle slightly different from 45 degrees so the effective focal planes line up in space. The appropriate correction depends on the details of the entire optical system and must be calculated for every focal plane. In this work the proximity of the two AOD devices and the small excursions from nominal focal plane make the astigmatism negligible relative to other sources of measurement error, so every plane is scanned at 45 degrees to simplify volume reconstruction.

### 2.2.4 Imaging Protocol

The protocol for imaging is the same for all acquisitions. The scan parameters used are $100 \times 100$ pixels, with a focal area of $102 \times 102$ $\mu$m$^2$. Each volume contained 10 focal planes, or slices, captured with a distance between them of 1

$\mu$m. An example of a single slice and $z$-projection is shown in Fig. 2.1 *B*. The data acquisition rate is set at 1 Mhz, so that with the time to fill the AOD the total acquisition time per volume is 86 ms. At these rates some slight "smearing" of the point spread function is apparent due to movement of the particle during the acquisition; this does not significantly affect the results of our analysis. Due to memory constraints on the oscilloscope used, 100 frames are collected before pausing to offload the memory, and then repeated 10 times for a total of 1,000 frames. Each 100 frame acquisition takes 8.6 seconds, follow by approximately 6 seconds spent clearing the oscilloscope memory. Therefore, for a full 10 repeat acquisition, the final observation occurs at 140 seconds. Throughout all experiments there are sufficient microspheres on a slide to image a single microsphere for one full scan, followed by focusing on a different particle. This minimized photobleaching, and assured a broad coverage of the available space for diffusion. Images are gathered for a maximum of 4 hours per slide, at which time diffusive motion is no longer evident. This is due to the microspheres sticking to the slide and coverslip, as can be seen by moving the focal plain to show immobile populations in each plane. While microspheres become stuck continually through the experiment, these are not tracked during the image analysis stage. No temperature control is used during the experiments. For all experiments room temperature is approximately 22 °C. Any small variation in temperature should have a small effect on the resulting behavior. Refering to Eq. 2.3, a difference of 1 K changes the diffusion constant by approximately 0.3%, which is well within experimental error.

### 2.2.5 Data Analysis

The resulting volumes are analyzed using the Imaris software suite (Bitplane, South Windsor, CT). A first pass of particle positions is automated by the software, using the internal particle tracking algorithm. This is followed by hand-picked filtering to eliminate extraneous points, and finally each frame is examined by eye to ensure proper positioning of particles. This step is very time consuming and is the limiting factor in obtaining the 3D particle trajectories used in this study. The resulting output consists of the $x$, $y$ and $z$ coordinates of each particle

$\mathbf{X}_i$ over time $t$. Example trajectories for each experimental condition is shown in Figs. 2.1, *C-E*. These trajectories are analyzed as described in the introduction.

### 2.2.6 Random Walk Model Simulation

Brownian motion and fractional Brownian motion processes are simulated to compare with the experimental results. A BM process is simulated as a solution to a Langevin equation

$$\mathbf{X}(t + \mathrm{d}t) = \mathbf{X}(t) + \mathbf{B}[\mathbf{X}(t)]\eta\sqrt{\mathrm{d}t} \tag{2.13}$$

where $\eta$ is Gaussian white noise with zero mean and unit variance, and $\mathbf{B}$ is a diffusion tensor, which in this case is diagonal and isotropic. fBM is characterized by zero mean, variance that scales algebraically, and a two-point correlation given in Eq. 2.10. fBM trajectories are generated using the Hosking method [56].

The diffusion constants chosen are informed from the experimental results reported below. In the case of BM, the diffusion constant used is $\mathbf{B} = 0.92\mathbf{I}$ where $\mathbf{I}$ is the identity matrix. In the case of fBM, $K_H = 0.02$. To calculate the correct value for $\mathbf{B}$ it is important to remember that the $D_\alpha$ reported in the experimental results is a 3D diffusion constant, where $\langle\delta^2\rangle = 6D_\alpha t$. This is in contrast to simulations of random walks in each coordinate direction, which has the relation $\langle\mathbf{X}(t)^2\rangle = 2D_\alpha t$. Therefore, to find $B$, we take the experimental value and multiply it by 2. This is not the case for fBM, where we directly use the value found in experiments. The fBM simulations are calculated with $H = 0.75$, again chosen based on the experimental results. For both BM and fBM, 30 trajectories are simulated for 500 time steps, similar to the data available from the experimental results. Simulations of CTRW are not performed because with time steps of varying length calculating a time-averaged MSD is unfeasible. All resulting trajectories are analyzed using the same methods as the experimental trajectories.

## 2.3 Results

### 2.3.1 Experimental Results

As described above, images are acquired under three distinct conditions: for microspheres in buffer, in a cellular extract with intact microtubules, and in a cellular extract treated with nocodazole where the microtubules are depolymerized. There are 28, 40 and 31 trajectories acquired for each case respectively. The time averaged MSD is calculated for each trajectory according to Eq. 2.5. These trajectories are ensemble averaged, and the resulting averaged trajectory is fit using Eq. 2.6. These average trajectories and the resulting fit parameters are shown in Figs. 2.2, $A$ and $B$ for short and long times. An important note is that the variance grows with lag time, as there are fewer segments to average over as lag time increases. This accounts for the poor fitting seen at large lag times, and is the reason the full trajectory of 140 seconds is not shown.

Looking at the buffer condition first, Eq. 2.6 is applied to both short and long lag time data to obtain $\alpha = 0.98$ and 1.12, respectively. This suggests normal Brownian motion, as expected for this case. Calculating the diffusion constant using Eq. 2.3 gives a diffusion constant of $D_\alpha = 0.24\ \mu\text{m}^2/\text{s}$, which matches well with the values of $D_\alpha = 0.42$ and $0.45\ \mu\text{m}^2/\text{s}$. The error most likely comes from uncertainty in position measurement during the image analysis phase.

For the extract condition, which captures cytoskeletal transport along microtubules, we find $\alpha = 1.48$ and 1.47 for the short and long lag time analysis. These values are consistent with the $\alpha = 1.47$ ($\pm 0.07$) reported in [25] (our $\alpha$ is equivalent to their $\gamma$). Furthermore, the fact that $\alpha$ does not appear to be a function of time suggests the observed superdiffusive behavior arises from long term correlations. Comparing the fit diffusion constant is inappropriate in this case due to the assumptions inherent to Eq. 2.3, namely that the observed particle is in a dilute suspension.

In the case of nocodazole treated extract, $\alpha = 0.65$ in the short lag time analysis, but $\alpha = 0.98$ is observed in the long time lag case. This transition from anomalous to classic Fickian diffusion has been observed previously, and

typically results from processes with a finite correlation length [71]. Because $\alpha$ is not a function of time in the extract case, this suggests these two processes are fundamentally different. There have been a number of recent studies of intracellular anomalous diffusion in which this transition has been noted [20, 119, 25, 128, 46]. These results also show that the diffusion constant $D_\alpha$ is smaller and similar in both extract cases compared to buffer, as would be expected for hindered diffusion. Again, comparision to Eq. 2.3 would be inappropriate.

### 2.3.2 Pre-ergodic Analysis

As suggested above, analyzing experimentally obtained particle trajectories in terms of their ergodicity could potentially distinguish what type of underlying processes govern diffusion in each of our experimental conditions. Several groups have investigated the ergodicity of random walk processes and shown differences in the distribution of time-averaged MSDs $\phi(\xi)$, which acts as a representation of the underlying ergodicity of the process [51, 77, 60]. We calculate the parameter $\xi_i = \overline{\delta_i^2}/\langle\delta^2\rangle$ for each experimental condition and plot histograms of the distributions at four lag times in Fig. 2.3. These snapshots at discrete lag times give a good idea of the shape of these distributions, and suggest that they each evolve differently with respect to lag time $\Delta$. To get a complete picture of the distribution with respect to lag time, the distribution for many values of $\Delta$ are plotted in Fig. 2.4. To help compare these figures, note that the $y$ axis for all plots in Fig. 2.3 corresponds to the heat values in Fig. 2.4, whereas the $y$ axis in Fig. 2.4, $\Delta$, is a fine discretization of the four lag times spanned in Fig. 2.3 from the top to bottom row. With this in mind, it is immediately clear that each condition shows markedly different statistics.

To categorize these distributions, the same statistics for random walk processes shown to result in anomalous diffusion are examined. Based on a comparison of the plots in Fig. 2.4 with previous work [59], we use CTRW with a power-law $\psi_{\Delta t}(\cdot)$ to model the free diffusion condition (extract + noc) and fBM to describe the cytoskeletal transport condition (extract). Both BM and fBM random walks are simulated, and the MSD is calculated for each resulting trajectory. The ensemble-

averaged MSD from these simulations is compared to the experimental results in Fig. 2.2 *C*, which shows excellent agreement between a BM process and the buffer case, and fBM and the extract case.

In addition, a distribution of time-averaged MSDs is calculated from the simulated trajectories. For the case of CTRW, an analytically derived distribution of time-averaged MSDs, Eq. 2.9, is used. Note that the distribution does not depend on lag time $\Delta$. Although this distribution assumes an infinite observation time, is has been shown that this result matches simulated data with a much shorter observation time, on the order of 100 time steps [59]. To aid visual comparison, Gaussian white noise ($\mu = 0$, $\sigma = 0.05$) is added on top of the distribution to simulate the noisy appearance. Using this analytic distribution and the simulated data, the distribution $\phi(\xi)$ is plotted as a function of lag time in Fig. 2.4. In the simulations of fractional Brownian motion $\alpha = 1.5$, as seen in the experimental data. For the CTRW distribution, a best fit is obtained with $\alpha = 0.6$. This value is motivated from the short lag time result, as it appears normal Fickian diffusion is recovered at long lag times, and we are interested in the anomalous behavior.

Examining the distributions of time-averaged MSDs and recalling that these distributions are analagous to ergodicity, the differences between these processes become clear. As seen in Fig. 2.4, for a BM process the distribution remains Gaussian and centered around $\xi = 1$ for all lag times, as expected. fBM is ergodic at short lag times with a peak centered at $\xi = 1$, and slowly shifting toward $\xi = 0$ with increasing lag time. This evolution of the distribution of time-averaged MSDs with lag time is similar to previously reported results looking at fBM with short observation times [59]. CTRW is a non-ergodic process which is characterized by a peak independent of lag time and shifted toward $\xi = 0$, and again was reported previously [51].

## 2.4 Discussion

Comparing the experimental and model plots in Fig. 2.4 similarities are immediately apparent. For free diffusion in a buffer, the distribution has the same

characteristics as a BM process. For the case of free diffusion in the extract after treatment with nocodazole, a shifted distribution that is independent of lag times is observed, similar to a CTRW process. An interesting facet of this result is that although we saw a transition from anomalous to Fickian diffusion in the MSD analysis, in the ergodicity analysis it appears there is no dependence on lag time. However, as we are analyzing these results in a pre-ergodic regime, this may simply reflect the lack of self-averaging achieved over the time period analyzed. Future investigation of this relationship may provide insight into the relationship between ergodicity and this transition. Finally, in the case of cytoskeletal transport along microtubules (extract), a distribution starting centered and slowly shifting toward zero with increasing lag time is seen. In the untreated extract case, one would expect free diffusion and cytoskeletal transport along microtubules to occur in concert, but the statistics suggest that cytoskeletal transport dominates in this experimental condition. The similarities to the simulated data are striking and illuminating. A word of caution: it is very important to recognize that there are a variety of random walk processes and the field remains rapidly evolving. We are not claiming that the intracellular processes are exactly represented by the described random walk processes, but simply that the statistics seen here appear to be well modeled by such processes.

The lack of consensus in the published literature suggests that intracellular transport is very complicated. Here, we have shown that cytoskeletal transport along a microtubule is statistically distinct from free diffusion within the cytosolic fraction examined. This result shows cytoskeletal transport is not simply diffusion with a higher diffusion constant, but a distinct process, providing a unique method for transport. This supports the idea that cytoskeletal transport is essential, as traditional diffusion would be unable to mimic this behavior. Furthermore, we have shown these process are well modeled by fBM and CTRW, respectively. Despite this success, there is still contrary evidence regarding the intracellular diffusion process. As already mentioned, both fBM [40] and CTRW [60] have successfully modeled experimental data from free diffusion in the cytosol. Our data and analysis suggests that CTRW is a more accurate model for intracellular free diffusion,

although the difference between our experiments on a slide and results from living cells may explain this discrepancy. Although they are instructive, the measures of diffusion used here, the scaling over time ($\alpha$) and a measure of ergodicity ($\xi$), provide an incomplete description of these processes. Organization and structure within cells likely has a major impact on transport, and improvements in tracking smaller particles in living cells, for extended observation times, will allow a more complete characterization of intracellular transport. However, the models proposed here present a powerful tool for beginning to understand these processes.

There are a few previous results that relate to what we have shown here. In this work the boundary effects present with cell membranes are not accounted for, yet previous work has shown that boundaries can have a non-negligible effect on random walk processes [93, 24]. Therefore, an important next step is to perform these experiments in vivo to properly account for these effects in experiments. Another recent study focused on the diffusion of membrane-bound proteins in migrating cerebellar granule cells; the authors observed a net forward transport towards the leading front [136]. This biased diffusion was modeled using Brownian motion with a drift component, despite the presence of "bursts" of biased motion in which the observed protein moved in the same direction for several consecutive steps. The similarity with our observations in the extract case suggests that an fBM process with positive correlation may provide an accurate model for the described behavior. An important distinction is their finding that the process is dependent on the motor protein myosin II, which interacts with actin filaments. In our case the transport appears to be microtubule mediated, but cytoskeletal transport on either actin or microtubules have similar mechanics, suggesting the models proposed here may be appropriate. Another intriguing result involves assuming the cytoskeletal transport is modeled by a fractional Brownian process, as suggested above. The Hurst exponent can be calculated for the cytoskeletal transport data to be $H = 0.75$ from the definition $\alpha = 2H$. The Hurst exponent is a measure of long term correlations in a time series [80]. Deng and Barkai found that the ergodic behavior of fBM is dependent on the Hurst exponent, and that a non-smooth transition occurs as $H \to 0.75$ [33]. While it isn't clear exactly how this detail effects the

physical process, it is intriguing. Future experiments and theory may shed light on whether this is important or merely a coincidence.

Understanding intracellular transport is essential to understanding complicated cellular processes. While there remain many questions, we have shown strong evidence that CTRW with power-law distributed temporal increments is a good model for intracellular free diffusion, and similarly fBM is a good model for cytoskeletal transport along microtubules. The fact that these are statistically distinct processes, as opposed to parametrically different examples of a single process, is an interesting and powerful result. Future studies exploring this result in vivo combined with extensive modeling will continue to improve the characterization of a variety of intracellular processes. These results also offer an interesting perspective on cellular processes that take place in the cytosol. Cells could be organized in a way that CTRW-like processes directly impact reaction processes, where the locally anomalous diffusion increases reaction rates by increasing the encounter rate. This increase in encounter rate emerges from the long waiting times that can occur in a CTRW process, keeping a molecule in a given local space longer than would be expected for a BM process. Opposing this is an fBM-like process that can act as a regulatory mechanism to transport proteins away from local traps and separate reaction partners as necessary. This idea is supported by the correlated stepping seen in fBM that could lead to a rapid removal of a molecule from a local space. The interplay of these processes would allow fine control over cellular processes without relying on organelles or membranes for segregation. Proving this interaction will require clever experiments to tease out the details, but the work presented here suggests the appropriate mechanisms exist.

In the following chapter we will analyze the data presented here using an algorithm based on a renormalization group operator for determining the anomalous diffusion exponent of single trajectories.

*Regner, B. M., Vučinić, D., Domnisoru, C., Bartol, T. M., Hetzer, M. W., Tartakovsky, D. M., Sejnowski, T. J., (2013). "Anomalous diffusion of single particles in cytoplasm". Biophysical Journal, 104(8), 1652-1660.*

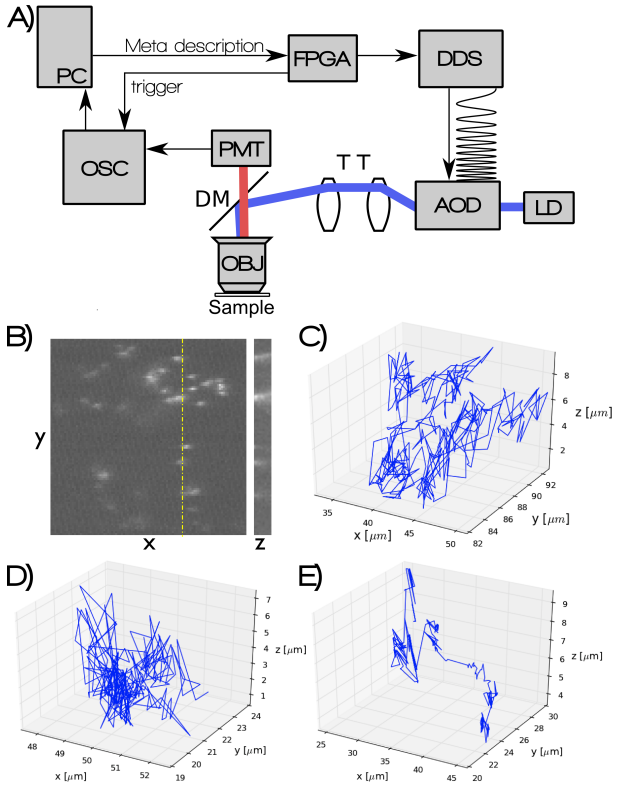


**Figure 2.1**: A) Block diagram of the microscope used in this work. Custom PC software controls all microscope functions and finalizes data acquisition. After scan parameters are entered, the scan program is sent to a field-programmable gate array (FPGA) as a meta language string of hexadecimal characters and saved into onboard memory. A start command is sent with the number of repeats to begin a scan by driving a direct digital synthesis (DDS) board, producing a series of frequencies and chirp rates directing the acquisition of the volume, while a concurrent trigger signal is sent to the data acquisition oscilloscope. A laser diode (LD) is directed by the acousto-optic deflectors (AOD), through a telescope tube (TT), and reflected by a dichroic mirror (DM) onto the back aperture of an objective (OBJ). The light emitted by the sample is collected on a photomultiplier tube (PMT) and converted into an image on the PC. B) Example image from the microscope. Note that high and low concentrations, as seen here, are common, and that all trajectories are taken from single molecules that never overlap. The broken line indicates the z cut shown to the right. C-E) Example trajectories of a bead in a C) buffer solution D) extract E) extract treated with nocodazole.

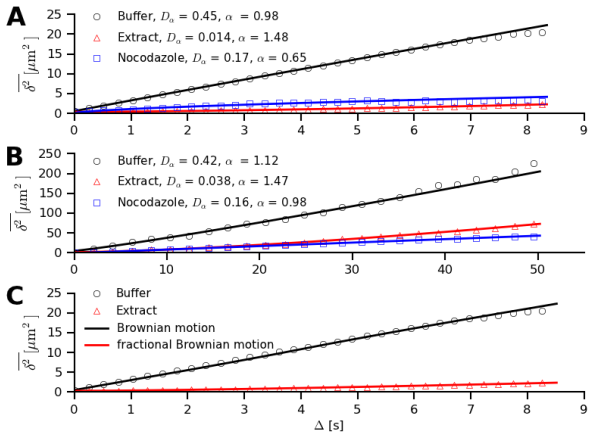


**Figure 2.2**: A,B) Comparison of averaged trajectories for diffusion in cellular extract, buffer solution, and cellular extract treated with nocodazole. A) Short lag time analysis. B) Long lag time analysis. C) Comparison of random walk models to experimental results. Note that a time-averaged MSD of CTRW trajectories is inappropriate, therefore there is no comparison to the experimental condition of extract with nocodazole.

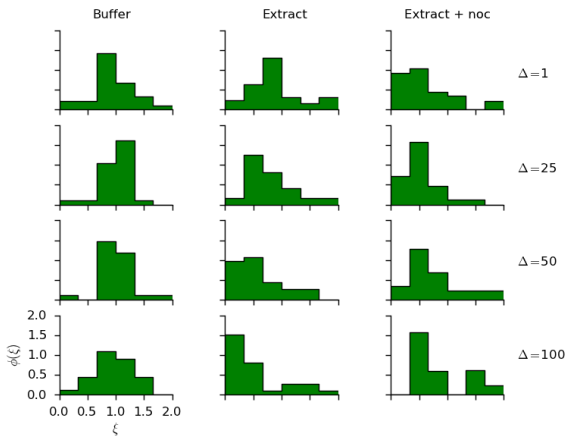


**Figure 2.3**: Snapshots of the distribution $\phi(\xi)$ for the three experimental conditions at four different lag times $\Delta$. In the case of buffer, 28 trajectories are analyzed, in the untreated extract case, 40 are analyzed, and in the case of extract treated with nocodazole, 31 are analyzed. All figure axes mirror those in the bottom left, but are removed for clarity. Note the trend in the case of buffer and extract+nocodazole is independent of lag time whereas the case of extract shows a shifting peak with increasing lag time. To see this trend more clearly, compare this figure with Fig. 2.4 which plots the distribution for many values of $\Delta$.

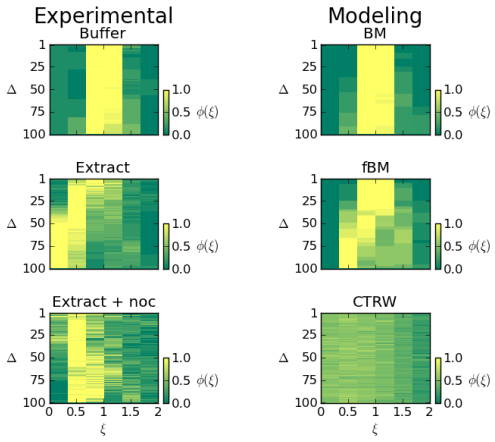


**Figure 2.4**: Comparison of distribution $\phi(\xi)$ for the three experimental and three modeling conditions. BM denotes Brownian motion, CTRW denotes continuous time random walk, and fBM denotes fractional Brownian motion. In the case of the experimental data, although there is noise due to the limited number of trajectories, the trends in each case are distinctive. Furthermore, the three modeling conditions shown are quite similar to the paired experimental conditions, suggesting these processes are good representations of the biological process.

# 3 Identifying Transport Dynamics of Single-Molecule Trajectories

## 3.1 Introduction

Stochastic fluctuations arise in biological systems at all length and time scales. An example is the diffusion of biomolecules, driven by thermal fluctuations, providing transport for biochemical processes. A familiar process that can generate such behavior is Brownian motion, although in biological systems the explicit assumption that particles are dilute is often violated. Diffusion processes that do not produce Brownian statistics are said to exhibit anomalous (non-Fickian) diffusion. Occurrence of anomalous diffusion has been reported in diverse phenomena, and has enriched understanding of biological systems [55].

Particle trajectories produced by single-molecule experiments are particularly suitable for characterizing biological diffusion behavior. A particle trajectory of length $M$ is represented by a sequence of time-ordered random variables $\mathbf{X} = \{X_i\}_{i=0}^{M}$, where $X_i = X(t_i)$ is the particle's location at time $t = t_i$. Anomalous behavior arises when a trajectory has non-zero drift, correlated increments, non-stationary increments, or some combination [99]. Equivalently, Brownian motion is observed when these conditions are absent. The trajectory of a particle undergoing Brownian motion exhibits a mean-square displacement (MSD) that grows linearly with time $t$. Anomalous diffusion typically produces an MSD, $\langle \mathbf{X}^2 \rangle$, that

is a nonlinear function of $t$, e.g. a power law

$$\langle \mathbf{X}^2 \rangle = D_\alpha t^\alpha, \qquad 0 < \alpha < 2. \tag{3.1}$$

Here $D_\alpha$ is the diffusion coefficient, and $\langle \cdot \rangle$ denotes an average over an ensemble of random trajectories. The process $\mathbf{X}$ is called subdiffusive if the exponent $\alpha < 1$ and superdiffusive if $\alpha > 1$ [18].

Although many experiments use MSD as a key statistic describing the observed dynamics, it might not be an appropriate metric for classification of stochastic trajectories. MSD-based classifications are often plagued by systematic [63] and localization [87] errors; fail to classify a broad class of processes whose dynamics are not Brownian but produce MSD growing linearly with time [99]; are problematic for analysis of microscopy experiments, which are often limited by short observation times and few captured trajectories [63], and cannot handle multiple transport mechanisms occurring over a given time span, e.g., on-off switching in cytoskeletal transport [5].

Renormalization group operators (RGO) can provide an alternative classification approach [99, 98]. A random trajectory $\mathbf{X}$ has a set of increments $\mathbf{I} = \{I_i\}_{i=0}^{M}$, with each increment computed as $I_i = X_{i+1} - X_i$. An RGO $R_{p,n}$ is defined by

$$(R_{p,n}\mathbf{I})_i \equiv \sum_{k=in}^{(i+1)n-1} \frac{I_k}{n^p}, \qquad p > 0, \qquad n \geq 1, \tag{3.2}$$

and a new replica trajectory $\mathbf{J}$ is determined as $J_i^{p,n} = (R_{p,n}\mathbf{I})_i$. A sequence $\mathbf{I}$ is called a fixed point of the RGO if for a fixed $p$, the relationship

$$\mathbf{J}^{p,n} \stackrel{d}{=} \mathbf{I} \tag{3.3}$$

holds for all $n \geq 1$, where $\stackrel{d}{=}$ means equal in distribution [111]. A process that is a fixed point with scaling $p$ is said to be a p-diffusive, or p-self-similar, and is related to the anomalous diffusion exponent by $\alpha = 2p$ [99]. Example replicas $\mathbf{J}^{p,n}$ are shown in Fig. 3.1, visually demonstrating replica trajectories that are a fixed point of Eq. 3.3. A generalization is a random renormalization group operator, in which

the scaling is a random variable $P$ [98]. In this framework, a single experimental trajectory is a realization of a process that samples a scaling distribution $f_P(p)$.

In this chapter, we propose an algorithm that compares replicas $\mathbf{J}^{p,n}$ with varying $n$ and uniformly distributed $p$ to the original trajectory $\mathbf{I}$ to determine a scaling distribution $f_P(p)$. The average scaling exponent for a single trajectory is given by $\alpha = 2\bar{p}$, where $\bar{p}$ is the mean of the empirical distribution $f_P$. The goal of this algorithm is to obtain $\bar{p}$ from single, short trajectories of experimental data; other methods may be more appropriate for analytic processes [100].

## 3.2 Methods

The proposed algorithm consists of the following steps:
First, a single trajectory $\mathbf{X}$ is transformed into the increment process $\mathbf{I}$. Second, an empirical cumulative distribution function (CDF), $F_I^0(x)$, of $\mathbf{I}$ is computed. Third, multiple realizations $p$ of a random variable $P$ equally spaced on the interval $[0, 1]$ are drawn, and multiple replicas of $\mathbf{J}^{p,n} = R_{p,n}\mathbf{I}$ are generated from Eq. 2 for a fixed $n$ and each $p$. Fourth, these replicas are used to compute $F_J^{P,n}(x)$, an empirical CDF of $\mathbf{J}^{P,n}$. Fifth, Kuiper's two-sample test is used to compare the CDFs $F_I^0(x)$ and $F_J^{P,n}(x)$ for each $p$, resulting in a goodness-of-fit statistic $g^{P,n} = \sup_x |F_I^0(x) - F_J^{P,n}(x)| + \sup_x |F_J^{P,n}(x) - F_I^0(x)|$ [74]. Sixth, the $p$ that results in the best (smallest) goodness-of-fit $g^{P,n}$ is stored for each $n$. These steps are repeated for many values of $n$ to obtain corresponding best-fit values of $p$ that are plotted as a histogram to obtain a distribution $f_P(p)$ for a given realization. Finally, the scaling exponent is computed as $\alpha = 2\bar{p}$, where $\bar{p}$ is the mean of the empirical distribution $f_P$; the corresponding diffusion coefficient is defined by $D_\alpha = \sigma_I^2/(2\delta t^\alpha d)$, where $\sigma_I^2(t)$ is the variance of $\mathbf{I}$, $\delta t$ is the time step and $d$ is the spatial dimension [85].

The use of increments $I_i^\Delta = X_{i+\Delta} - X_i$ for a lag time $\Delta$ (the number of time steps) improves estimation of $D_\alpha$. The diffusion coefficient is then calculated as

$$D_\alpha = \frac{1}{M}\sum_{\Delta=1}^{M} \frac{\sigma_{I_\Delta}^2(t)}{2d(\Delta\delta t)^\alpha}. \tag{3.4}$$

This calculation also acts as an indicator of the accuracy of the calculated scaling. If an estimate of $\bar{p}$ is inaccurate, then $D_\alpha(\Delta)$ will change significantly with $\Delta$, indicating a poor fit.

A trivial extension is to perform the operation over a population of trajectories, and to produce an ensemble histogram for the population. An ensemble distribution is analogous to previous methods of computing the scaling, but has the advantage that each trajectory is treated individually, a fact particularly useful when the population contains a mix of processes. A further refinement is to break each trajectory into subtrajectories, and treat each as an independent trajectory. If the trajectories are stationary and ergodic, a good approximation of the distribution $f_P(p)$ results. Otherwise, the method may provide a way to analyze nonstationarity and ergodicity breaking of stochastic processes.

The RGO can be thought of as "resampling" of the probability space $(\Omega, \mathcal{U}, \mathcal{P})$. Given a sequence of independent identically distributed (i.i.d.) random variables $\mathbf{X} \in \Omega$, the RGO provides a means of properly constructing a new sequence of i.i.d. random variables $\mathbf{X}' \in \Omega$, improving the ability to classify the sampled probability space. The MSD calculation only considers the statistical information in the original sequence, and therefore requires averaging across realizations to cover the probability space. In contrast, new sequences constructed using the RGO extract a maximum of statistical information from the given realization. While this does not ensure coverage of the probability space, it is an improvement relative to the MSD method.

## 3.3 Results

### 3.3.1 Validation on Simulated Data

To demonstrate the efficacy of our classification algorithm, we use it to analyze data generated by fractional Brownian motion (fBM), a diffusion process often used to model anomalous behavior. It is denoted $\mathbf{B}^H$ and defined with initial condition $B_0^H = 0$, zero mean $\langle \mathbf{B}^H \rangle = 0$, and a two-point correlation $\langle \mathbf{B}_t^H \mathbf{B}_s^H \rangle = (|t|^{2H} + |s|^{2H} - |t-s|^{2H})/2$ where $H$ is the Hurst exponent. It can be shown

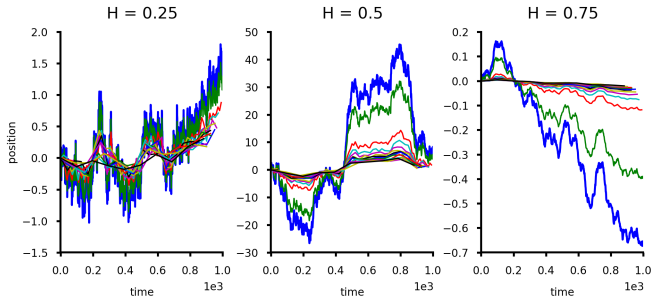


**Figure 3.1**: Three examples of fractional Brownian motion (dark blue) with example replicas for multiple values of $n$ (multiple colors). The replica trajectories are a fixed point of the proposed renormalization group operator with $p = H$.

that $\mathbf{B}^H$ is a fixed point of Eq. 4 with $p = H$. Therefore, a proper classification algorithm should yield a distribution $f_P(p)$ centered around the mean $\bar{p} = H$.

We simulate ten realizations of $\mathbf{B}^H$ with $H = 0.25$ and 0.75, for 1000 time steps, using the circulant method as implemented in the R package dvfBm [140, 27]. Their representative distributions $f_P$ are shown in Figs. 3.2(a) and (b) for $H = 0.25$ and $H = 0.75$, respectively. In all cases good agreement with the scaling of the underlying process is observed. The exact scaling, $\delta(x - P)$ where $\delta$ is the Dirac delta function, is replaced with a finite-width distribution that accounts for uncertainty introduced by the trajectory's short length. An ensemble histogram of the population of ten trajectories with $H = 0.25$ in Fig. 3.2(c) shows weak convergence to the expected mean. A mixed population of ten trajectories from each $H$ in Fig. 3.2(d) demonstrates that the algorithm robustly recovers a bimodal distribution for the mixed case. MSD methods are unable to replicate this result, while Bayesian methods require the use of mixture models, which can be difficult to implement [98, 82].

### 3.3.2 Application to Experiments

The validated classification algorithm is used to analyze previously reported data [106]. Briefly summarizing, we obtained 3D particle trajectories of a fluorescent microsphere, diameter 1 $\mu$m, diffusing in a cellular extract prepared from

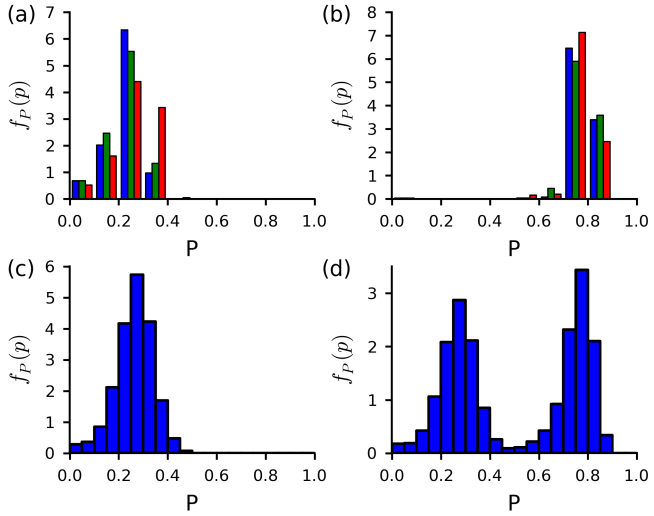


**Figure 3.2**: Ten trajectories of a fractional Brownian motion $\mathbf{B}^H$ are simulated for $H = 0.25$ and $H = 0.75$ over 1000 time steps. Our algorithm is applied to these trajectories to obtain distributions of the critical exponent $P$. (a) and (b) Single trajectory histograms for $H = 0.25$ and $H = 0.75$, respectively. (c) Ensemble histogram from a population of ten trajectories with $H = 0.25$. (d) Ensemble histogram of all trajectories combined, revealing an expected bimodal distribution that MSD would fail to detect.

*Xenopus* oocytes. Another set of trajectories was also obtained from the same extract treated with nocodazole, which is known to depolymerize microtubules. Previously, an MSD-based analysis using Eq. 3.1 classified transport as superdiffusive along microtubules in the extract case ($\alpha = 1.5$ for both short and long times; and $D_\alpha = 0.014$ and 0.038 in short- and long-time analyses). The units for all experimental diffusion coefficients are $\mu m^2/s^\alpha$, in agreement with Eq. 3.1. Addition of nocodazole led to subdiffusive transport at short times ($\alpha = 0.6$), and classical diffusion ($\alpha = 1.0$) at long times; in both cases, $D_\alpha = 0.16$ [106]. Figure 3.3 exhibits the resulting MSDs.

Figure 3.4 presents the results obtained with our classification algorithm for the extract (left column) and nocodazole (right column) cases. Distributions from single representatives trajectories are shown in Figs. 3.4(a) and (b). Both cases exhibit superdiffusive and subdiffusive signatures, though they are less evi-

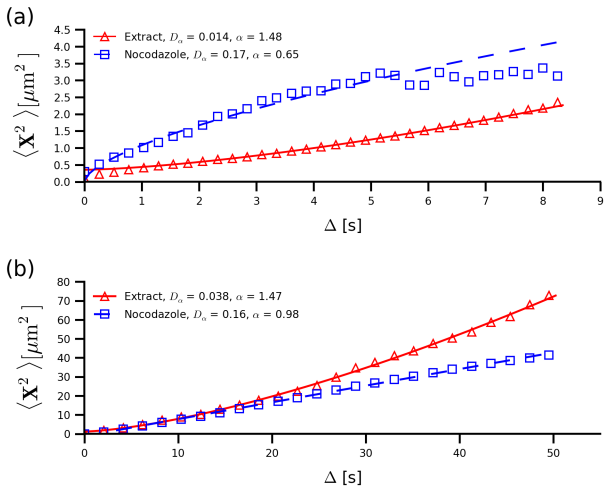


**Figure 3.3**: (a) At short times, transport is superdiffusive in the extract case (due to active transport along microtubules) and subdiffusive in the nocodazole case. (b) At long times, transport is superdiffusive in the extract case and Fickian in the nocodazole case.

dent in the nocodazole case. This behavior in the extract case is to be expected, as the dynamics of microtubule transport include rapid switching between on and off states [5]. The MSD classification misses this phenomenon, classifying the transport as superdiffusive. Superdiffusive transport in the nocodazole case suggests incomplete depolymerization of the microtubules, which remained undetected by the MSD analysis. Fig. 3.4(c) and (d) show ensemble population distributions, with $N = 38$ in the extract case and $N = 19$ in the nocodazole case. In the extract case, multiple scalings occur during the time course of the collected data. The ensemble distributions reveal that in the case of nocodazole, while the majority of trajectories undergo subdiffusion, there is a strong signature of superdiffusive transport.

Table 3.1 contains the values of the diffusion coefficient $D_\alpha$ computed with Eq. S1. The MSD and RGO methods predict similar values of $D_\alpha$, with the small disagreement attributed to the MSD's use of Eq. 3.1, in which $D_\alpha$ is sensitive to the fitting of $\alpha$.

**Table 3.1**: Diffusion coefficients calculated with the MSD and RGO methods for different time windows. Units are $\mu m^2/s^\alpha$.

| | Short time $D_\alpha$ | | Long time $D_\alpha$ | |
|---|---|---|---|---|
| | MSD | RGO | MSD | RGO |
| Ext | 0.014 | 0.029 | 0.038 | 0.046 |
| Noc | 0.16 | 0.043 | 0.17 | 0.126 |

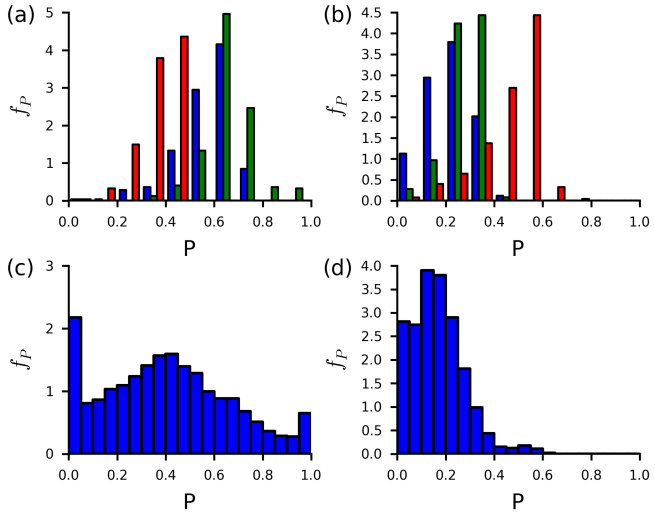


**Figure 3.4**: (a) and (b) Representative histograms of the empirical scaling distribution $f_P(p)$ of individual trajectories from the extract and nocodazole cases, respectively. Three examples are shown with each color indicating results from a single trajectory. (c) and (d) Ensemble histograms for the two cases. In the extract case, subdiffusive behavior is observed, which was not indicated by the MSD analysis. Similarly, weak superdiffusive behavior is observed in the nocodazole case, suggesting incomplete depolymerization of microtubules. The large mass at $P = 0$ arises from noise.

## 3.4 Conclusions

We have shown that renormalization group operators accurately classify processes with known scaling, and reveal rich dynamics in experimental data that is misinterpreted by MSD. The analysis presented in this chapter suggests that

while fluctuations in short-time windows can produce "improbable" sequences that scale differently from the underlying process, their average behavior is sufficient to correctly estimate the scaling exponent and to classify the process. Many biological phenomena are characterized by broad distributions for which it may be difficult (or even inappropriate) to assign a single value of the scaling exponent $\alpha$. This reflects the presence of multiple transport mechanisms (e.g., free diffusion, varieties of cytoskeletal transport, and active transport through pores) that may act upon biomolecules during different time windows or events [42]. From a regulatory perspective, diverse transport mechanisms with different scaling would provide a powerful means of control over biochemical pathways. The assortment of scalings seen in Fig. 3.4 is evidence of diversity in microtubule transport. The MSD analysis of individual trajectories of diffusing chromosomal loci [58] provides further support for this conclusion. The MSD-based estimates of the scaling exponents for individual trajectories were collected into a histogram shown in Fig. 2a of [58]. It is similar to the histogram for the extract case shown in Fig. 3.4(c). The proposed algorithm could also be used to classify the distinct short-time diffusive behaviors observed in different subcellular regions reported by [58], and to analyze rare events without ensemble averaging.

In summary, we developed a classification technique to analyze a short trajectory of a single biomolecule. It employs a renormalization group operator (RGO) [99], and allows computing both the anomalous scaling exponent and diffusion coefficient of a biomolecule's motion. The RGO-based classification alleviates key impediments to accurate identification of anomalous transport, which stem from scarcity of observed biomolecule trajectories, short duration of observation, and measurement errors, which render classifications based on the mean-square-displacement (MSD) calculations unreliable. After validation on data generated with fractional Brownian motion, we used the new method to analyze trajectories of diffusing microspheres observed in several biological environments. The RGO approach identified multiple transport processes that affect the observed particle migration, which were not apparent with the MSD-based method.

# 4 Monte Carlo Simulations of Hard Sphere Hydrodynamics

## 4.1 Introduction

Biological systems are characterized by broad heterogeneity in spatial and temporal scales with many degrees of freedom, in which a multitude of interacting parts work in concert to perform a given function. Describing these systems with general concepts and mathematical modeling is a daunting task. Computational simulations and modeling are powerful tools in making analysis of these complex systems tractable. A broad class of problems that fit this description are the many interconnected biochemical pathways underlying cellular function [5].

A number of simulation environments have been developed for spatially modeling biochemical networks, typically using either particle-based or lattice-based methods [69]. Many familiar problems in engineering are adequately handled by lattice-based methods, but advantages of particle-based methods in biology include relatively small numbers of particles, the ease of computing fluctuating concentrations, and the presence of complex geometries that are difficult to mesh volumetrically. Particle-based methods have been used successfully in modeling a variety of biological processes [124, 28, 118, 36]. However, the majority of simulation environments use point-particle representations.

As has been discussed in previous chapters, macromolecular crowding is often present in biological systems, and has a significant effect on the transport and reaction dynamics [88, 141]. Although complex geometries can be explored using point-particle representations, the effects of macromolecular crowding are absent.

Recently, efforts have been made to investigate diffusive behavior with crowding. For example, Sun et al. used an elastic collision model combined with a mean field hydrodynamic interaction model to show how diffusion and reaction kinetics change with volume fraction [126]. Ridgway et al. investigated reaction-diffusion dynamics using a hard sphere particle representation. They used a distribution of molecule sizes from the cytosol of the bacteria *E. Coli* to inform their model, giving them a uniquely cell-like environment compared to previous work [108]. Ando and Skolnick used similar methods to Sun et. al. while introducing more complex molecular shapes and comparing to simulations using only spherical representations. They showed that spheres provide an accurate approximation for globular proteins [6]. These studies have shown the importance of including crowding in computational models, but we are unaware of any general simulation environment that solves diffusion-reaction equations and accounts for particle size within an arbitrary geometry. The aim of the work proposed here is to implement hard sphere representations of particles in the MCell simulation environments.

MCell is a Monte Carlo simulator of diffusion-reaction systems in complex geometries. Currently, all volumetric particles are treated as point particles. In a given time step, a particle performs a ray trace to determine intersections with other particles and boundaries. Interactions with volumetric particles are determined based on a fixed interaction radius, while the boundaries are defined by the user. Reactions can be set for both particles and boundaries, and are probabilistically resolved. Further details can be found in [123, 64]. In order to investigate crowding, we began implementing a hard sphere particle representation using the Bullet physics engine.

In this work, we replace the ray tracing algorithms used in MCell with those available in the Bullet physics engine. Bullet is a multiphysics engine that can perform Newtonian dynamics with accurate collision detection [30]. The library is split into dynamics and collisions components, facilitating implementation of collision detection for complex shapes into MCell. In a given time step, Bullet determines for each particle a list of interactions using a convex cast, the equivalent of a ray trace for an object with finite size, which are subsequently handled by

MCell. An example is shown in Figure 4.1. Hydrodynamic interactions also play a crucial role in mesoscale simulations, particularly as the volume fraction approaches the percolation threshold [126]. In the proposed implementation, we make a mean field approximation of hydrodynamic interactions by measuring the local volume fraction and modifying the diffusion step length at each time step.

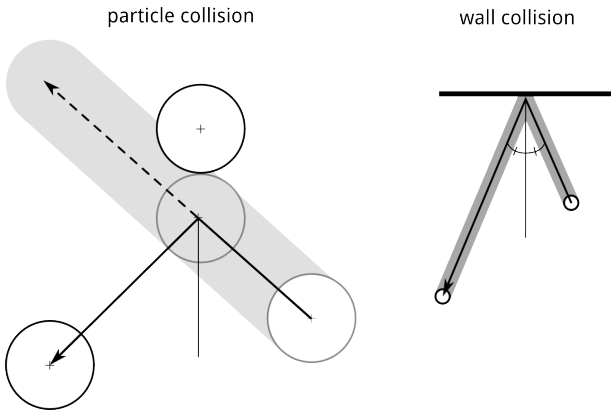


**Figure 4.1**: Examples of a ray trace (black line) and convex cast (shaded gray) for particle and wall collisions.

## 4.2 Methods

Implementation of hard sphere particle interactions using the Bullet physics engine is the main contribution in this work. A main problem to address is how to handle particle interactions with the introduction of finite size particles. Analogous to MCell, intersections with the boundary can either reflect, freely cross, react with surface particles or absorb. Intersection with another volumetric particle will either lead to reflection or initiate a probabilistic reaction event if the particles can react. With the introduction of hard sphere particles, handling the placement of reaction products requires a clear set of rules.

A limit on reactions is that only two products are allowed. While reactions with multiple products are both physically possible and essential for certain processes, typically a series of equivalent reactions producing short-lived intermediates can be used to mimic this behavior [64]. There are four possibilities with

two reactants and two products. There are two bimolecular reaction cases, when two volumetric particles collide. In the case of $A + B \to C$, the product is placed at the location $A$ and $B$ collided. In the case $A + B \to C + D$, the reactants $A$ and $B$ are replaced by the products $C$ and $D$, and the choice of which product replaces which reactant is chosen at random. There are also two unimolecular cases, decay of $A \to B$ in which the product replaces the reactant, and $A \to B + C$, which is a nontrivial case. In this case, a center location is fixed as the center of $A$. A random orientation vector is chosen, and the two products are placed a distance of $r_B + r_C + r_{tol}$ apart, where $r_{tol}$ is a tolerance to ensure they don't overlap within numerical precision. If the products cannot be placed without overlap due to crowding, a new orientation vector is generated at random. The user can specify how many times placement should be attempted before the reaction is considered blocked, and $A$ remains in place. A count of all blocked reactions is kept and reported at the end of the simulation. Surface reactions are handled similarly, with the products moved away from the wall one radius. Again, overlaps are checked to handle cases of narrowly separated boundaries, with overlap leading to a blocked reaction.

Hydrodynamic interactions are handled by a mean field approximation that previously has been shown to agree well with theoretical and experimental results [126, 130, 54]. The scheme adjusts the diffusion step length for each particle at each time step by computing local crowding information. First, all particles within two radii and four radii of the center of the particle of interest are found, e.g. Figure 4.2. If a particle $j$ is found within two radii of the diffusing particle $p$, a separation distance is calculated $d = l_{pj} - r_p - r_j$. The effective diffusion coefficient is modified by $D_{\text{eff}}(u) = D_0/\beta(u)$ where

$$\beta(u) = \frac{6u^2 + 13u + 2}{6u^2 + 4u}, \tag{4.1}$$

$D_0$ is the prescribed molecular diffusion coefficient and $u$ is a nondimensional distance $u = d/r_p$ [130]. If more than one particle is within two radii, the closest is used for the calculation.

If there are no particles within two radii, we compute the local volume fraction $\phi_l$ based on the total volume occupied by other particles within four radii.

The diffusion is altered by the factor

$$D_{\text{eff}}(\phi_l) = D_0 / \left[1 + \frac{2b^2}{1-b} - \frac{c}{1+2c} - \frac{bc(2+c)}{(1+c)(1-b+c)}\right] \tag{4.2}$$

where $b = (9\phi_l/8)^{1/2}$ and $c = 11\phi_l/16$ [126]. Only the overlapping particle volume is used in the computation of $\phi_l$ (light shaded region in Figure 4.2).

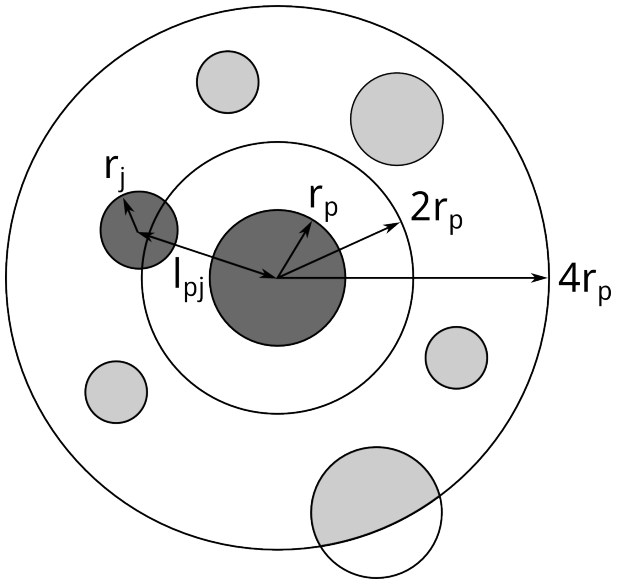


**Figure 4.2**: Diagram of a scheme for approximating hydrodynamic interactions. Given a particle of radius $r_p$, if another particle is within $2r_p$, the next diffusion step is adjusted using (4.1). An example is the particle with dark shading. If no particle is found in this range, the local volume fraction is computed using the volume occupied within four radii, and the correction factor is computed using (4.2). Examples of the volume used for this calculation are lightly shaded.

## 4.3 Results

While validating the implementation of the modeling described above, results for an effective diffusion coefficient at increasing volume fraction diverged from the expected result. After several attempts to track down possible bugs, this problem led to a deeper literature review in which we found references mentioning the importance of simultaneous time stepping for Brownian dynamics simu-

lations [125]. In such a time stepping scheme, all particles are moved forward in time until the first collision is detected. After handling this interaction, all particles continue on their path until the next collision, etc. In MCell, time stepping is performed with a queue in which a given particle completes its motion for a single time step in one continuous path. By maintaining a short time step, this approximation is acceptable in the case of point particles. Although we are performing probabilistic simulations compared to the Newtonian dynamics performed in Brownian dynamics simulations, by introducing hard sphere interactions, the importance of the time stepping algorithm becomes more pronounced.

Despite having a solution to this problem in hand, we decided to shelf the work until the current refactoring of the code base is completed. Ongoing efforts by the MCell development team are fundamentally changing the code from a monolithic simulator to a set of interacting modules. When complete, it will be significantly easier to change the time stepping algorithm compared to the current code structure. The majority of the code for hard sphere interactions is ready, and will be fully implemented later this year as the new MCell library nears completion.

# 5 Discrete Modeling of Effective Diffusion

## 5.1 Introduction

### 5.1.1 Modeling Biological Tissues

The brain exhibits structural heterogeneity across many length scales, and hosts dynamical processes that act across many time scales. Combined with the brain's brittle structure that is easily damaged by invasive methods, this heterogeneous multiscale behavior makes the brain notoriously difficult to observe [61]. Noninvasive imaging modalities, such as electroencephalography (EEG), magnetoencephalography (MEG), positron emission tomography (PET) and magnetic resonance imaging (MRI), collect continuum-scale data with limited spatial resolution [31]. Relating these continuum-scale measurements to pore-scale geometry remains an active research question. This chapter deals with quantitative analysis of neural tissue at cellular (pore) and tissue (continuum) scales, both of which are critical to understanding neural systems and producing accurate models of brain activity. We use a computational reconstruction of fixed brain tissue from rat hippocampus to begin elucidating the relationship between the pore and continuum scales.

The hippocampus, a highly heterogeneous region of the brain, plays a vital role in semantic and episodic memory and is strongly susceptible to diseases [120]. The scale of hippocampal subregions is on the order of centimeters, while the cell bodies and processes are on the order of microns, a difference in scale of four

orders of magnitude. Evidence suggests that local cellular connectivity is critical to understanding neuronal firing patterns [122]. Coupling pore-scale measures of diffusivity to continuum-scale processes is crucial for inferring the functionality from continuum-scale measures of activity.

While continuum-scale models are of practical importance and can be parameterized/validated by gross (continuum-scale) measurements, they rest on a number of assumptions and simplifications and employ largely phenomenological equations. In contrast, descriptions of dynamics at the pore scale are derived from first principles but suffer from epistemic uncertainty that reflects the scarcity or absence of pore-scale data. Furthermore, pore-scale models are computationally intractable when conducted over a tissue-scale domain. In response to these problems, a variety of upscaling methods have been proposed to couple these scales, improving continuum scale models through knowledge of the pore scale. Methods include volume averaging [138], homogenization by multiple-scale expansion [4] and pore-network models [3]. An overview of these and other upscaling methods can be found in [13]. In all cases, assumptions are made in the derivation of the upscaling procedure and care must be taken to ensure they are met to obtain accurate results.

All upscaling methods require knowledge about the pore space to inform the model, although obtaining an accurate pore-scale description can be difficult. In the case of biological tissue, the heterogeneity is at the nanoscale. The main imaging modality for resolving features at this scale is electron microscopy (EM), which requires chemical or cryogenic tissue fixation, This precludes dynamic analysis, such as temporal variability of concentration and species diffusivity. Mathematical modeling is used to reconstruct the dynamic nano-scale behavior of tissue from a series of electron micrographs. Figure 5.1 provides an example of such a reconstruction of rat neural tissue [67], which was collected in the hippocampus CA1 neuropil in the region stratum radiatum.

The reconstruction procedure used in [67] consists of the following steps. First, a standard protocol for perfusion and fixation is followed to prepare the brain before slicing. Second, serial-sectioning is performed on the resulting tissue block

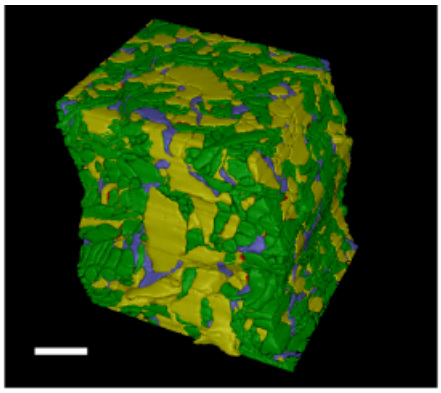

**Figure 5.1**: Image from the computational reconstruction of rat neural tissue with approximate dimensions $5 \times 5 \times 6$ $\mu$m$^3$ [67]. Identified cell types include axons (green), dendrites (yellow) and astrocyte (blue). Although not visually apparent, extracellular space occupies 20% of the volume. The reconstruction is a surface mesh generated from cell body contours. The contours are obtained from a series of 100 images with a spacing of 45-50 nm in the $z$ direction between slices.

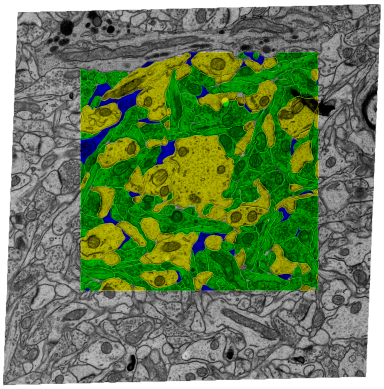

**Figure 5.2**: A representative example of the electron micrographs used for the computational reconstruction and the process of image segmentation. The color of the cell types is the same as Figure 5.1. The contours indicated are matched up with contours from slices above and below to obtain the 3D representation of every cell in the volume.

to produce an ordered series of sections. Third, these sections are scanned on a transmission electron microscope and compiled into a stack of images. The data set in [67] contained 160 slices with 45-50 nm separation in the $z$ direction between them; 100 slices were used in this reconstruction. Fourth, each image is segmented by hand to produce a stack of cell outlines or contours (an example is shown in Figure 5.2). Fifth, these contours are connected using computational algorithms to produce a three-dimensional surface mesh. Finally, refinement is performed to ensure the mesh is computationally viable and to correct for fixation artifacts such as compression and stretching. The resulting mesh in [67] has dimensions of approximately $5 \times 5 \times 6$ $\mu$m$^3$, and is assumed to be representative of a typical geometry in CA1.

We use homogenization by multi-scale expansion to determine an effective diffusion coefficient in this tissue. This diffusion coefficient provides a good approximation of the tissue-scale dynamics in the CA1 region of the hippocampus. Comparison with other regions is necessary to determine the generality of the result.

## 5.2 Diffusion Equations at Pore and Tissue Scales

Consider a macroscopic tissue domain of volume $V$. The tissue consists of the solid phase (cells) $V_s$ and the liquid phase (extracellular space) $V_l$, such that $V = V_s + V_l$. The liquid-solid interface is denoted by $\Gamma_{ls}$. Continuum-scale (macroscopic) descriptions of porous media, including tissues, rely on the concept of a representative elementary volume (REV) $\Omega$ that is large enough to average-out the effects of individual pores but is small enough to allow for macroscopic variability of the tissue. If the REV $\Omega$ consists of the solid phase $\Omega_s$ and the extracellular space $\Omega_l$, then the porosity $\phi$ of the tissue is defined as

$$\phi = \frac{V_l}{\Omega_s + \Omega_l}. \tag{5.1}$$

Diffusion through the tissue is modeled at two scales. The microscopic (pore) scale has a characteristic length $l$ representing, e.g., a typical dimension of the extracellular space; a microscopic (pore-scale) model of solute diffusion through

the tissue requires on to resolve the pore geometry and to solve a diffusion equation in the highly irregular (and possibly multi-connected) extracellular space $\Omega_l$. The macroscopic (continuum) scale has a characteristic length $L$ corresponding to the size of tissue under investigation; a macroscopic (tissue-scale) model of solute diffusion treats the tissue as a continuum composed of a single phase and involves solving an effective diffusion equation in a regular domain $V$ (e.g., a cube). The two scales satisfy a condition $\epsilon = l/L \ll 1$. The upscaling procedure requires one to assume that the pore-scale geometry is is composed of periodically repeated REVs that form "unit cells", but it also provides adequate representation of effective (upscaled) processes in disordered domains lacking periodic structure [14, 94].

The microscopic molar concentration $c(\mathbf{x}, t)$ of solute within the extracellular space $\Omega_l$ satisfies a diffusion equation

$$\frac{\partial c}{\partial t} = D_m \nabla^2 c, \qquad \mathbf{x} \in \Omega_l \tag{5.2}$$

where $D_m$ is the molecular diffusion coefficient for a species in the free extracellular fluid. This equation is subject to an appropriate initial condition and the boundary condition on the outer surface of the tissue volume $V$. It is also subject to a boundary condition on the internal liquid-solid interface,

$$-\mathbf{n} \cdot \nabla c = 0, \qquad \mathbf{x} \in \Gamma_{ls}, \tag{5.3}$$

which reflects the fact that the latter is impermeable to diffusion. Here $\mathbf{n}$ is the unit normal vector to the surface $\Gamma_{ls}$.

The macroscopic molar concentration $C(\mathbf{x}, t)$ of solute within the tissue $V$ satisfies a diffusion equation

$$\frac{\partial \phi C}{\partial t} = \nabla \cdot (\mathbf{D} \nabla C), \qquad \mathbf{x} \in V \tag{5.4}$$

where $\mathbf{D}$ is the effective diffusion coefficient tensor. This equation is subject to an appropriate initial condition and the boundary condition on the outer surface of the tissue volume $V$. The fundamental difference between the diffusion coefficients in (5.2) and (5.4) is worthwhile emphasizing. The molecular diffusion coefficient $D_m$ is a unique property of the solute and solvent; it is readily measured and (for

a given temperature) is likely to be a scalar constant. In contrast, the effective diffusion coefficient $\mathbf{D}(\mathbf{x})$ is a space-varying tensor, which captures not only the diffusive properties of the solute and solvent but also those of the tissue. The latter include tissue anisotropy and heterogeneity.

Upscaling allows one to relate the effective diffusion coefficient tensor the pore geometry of a tissue. We accomplish this by homogenizing the pore-scale diffusion equation (5.2) via an asymptotic series expansion in powers of $\epsilon$. The approach is based upon an assumption that the tissue is composed of a periodic arrangement of unit cells $\Omega$, the introduction of a fast space variable $\mathbf{y} = \mathbf{x}/\epsilon$, and the representation of the pore-scale concentration $c$ as an asymptotic series in powers of $\epsilon$,

$$c(\mathbf{x}, \mathbf{y}, t) = \sum_{m=0}^{\infty} \epsilon^m c_m(\mathbf{x}, \mathbf{y}, t) \tag{5.5}$$

where each $c_m(\mathbf{x}, \mathbf{y}, t)$ is $\Omega$-periodic in $\mathbf{y}$. This procedure allows one to express the diffusion tensor $\mathbf{D}$ in (5.4) as [14, 7]

$$\frac{\mathbf{D}}{D_m} = \mathbf{I} + \frac{1}{\Omega_l} \int_{\Gamma_{ls}} \mathbf{n}\mathbf{b} \mathrm{d}A \tag{5.6}$$

where $\mathbf{I}$ is the identity matrix and a "closure variable" $\mathbf{b}(\mathbf{y})$ is strictly a function of the pore-scale geometry. It is an $\Omega$-periodic vector field that satisfies a unit-cell problem

$$\nabla^2 \mathbf{b} = 0, \quad \mathbf{y} \in \Omega_l; \qquad \mathbf{n} \cdot (\mathbf{I} + \nabla \mathbf{b}) = 0, \quad \mathbf{y} \in \Gamma_{sl}. \tag{5.7}$$

A similar homogenization procedure can be carried out to upscale pore-scale biochemical reactions [14]. We focus solely on diffusive transport to elucidate the nature of the effective diffusion coefficient tensor.

### 5.2.1 Particle-based Solution of the Unit-Cell Problem

Given the complex geometry of the extracellular space $\Omega_l$, mesh-based (Eulerian) numerical solutions of the unit cell problem (5.7) would require a fine numerical mesh and can become computationally prohibitive. Instead, we implement

a mesh-free particle-based method to solve three scalar Neumann problems corresponding to (5.7),

$$\nabla^2 u = 0, \quad \mathbf{y} \in \Omega_l; \qquad \mathbf{n} \cdot \nabla u = f, \quad \mathbf{y} \in \Gamma_{sl} \tag{5.8}$$

where $u(\mathbf{x})$ stands for the $b_1$, $b_2$ or $b_3$ components of the vector $\mathbf{b}$, and the source $f(\mathbf{y})$ represents the corresponding components of the unit normal vector $\mathbf{n}(\mathbf{u}) = (n_1, n_2, n_3)^\top$. A probabilistic solution to the Neumann problem (5.8) is given by [21]

$$u(x) = \lim_{T \to \infty} \mathbb{E}_x \int_0^T f(X_s) dL_s \tag{5.9}$$

where $X_s$ is a reflecting Brownian motion (RBM) and $L_s$ is the local time on the boundary. This formulation is analogous to the Feynman-Kac representation of parabolic PDEs [41]. An RBM is a stochastic process with a transition density function $p(t, x, y)$ that satisfies

$$\frac{\partial p}{\partial t} = \frac{1}{2} \nabla^2 p, \quad \lim_{t \to 0} p = \delta_y(x), \quad \frac{\partial p}{\partial n} = 0 \tag{5.10}$$

This process remains in a closed domain by reflecting back into the domain when the path intersects the domain boundary. The local time is defined as

$$L_s(t) = \lim_{\epsilon \to 0} \frac{1}{\epsilon} \int_0^t \mathbb{I}_{D_\epsilon}(X_s) ds \tag{5.11}$$

where

$$D_\epsilon = \{x \in \bar{D} : d(x, \partial D) \leq \epsilon\} \tag{5.12}$$

and $d(x, \partial D)$ is the shortest distance between $x$ and the boundary. The local time is the time the RBM has spent on the boundary. Estimating these functions is critical to generating an accurate estimate of (5.9)

Recently, Monte Carlo estimation of the local time was done by projecting the position of the random walk onto the nearest wall and weighing the added local time using a delocalization parameter with a Gaussian kernel [79]. An advantage to this strategy is the ability to calculate the solution away from the boundaries, but in our case this is an unnecessary complication, as we only need the solution at the boundary. The strategy we employ is to estimate the local time by keeping track of each intersection a random walk makes with a face composing the boundary

during a single time step $dt$. We increment only once even if the random walk reflects back into that face a second time during a single time step. Note that if the time step is small enough, this is never a problem, but we impose this condition for completeness. We obtain the solution $\mathbf{b}_i$ for each face $i$ by

$$\mathbf{b}_i = \frac{1}{N} \sum_{k=0}^{T/dt-1} \mathbf{n}_i \mathbb{I}(k) dt, \; i \in \Gamma_{ls} \tag{5.13}$$

where $N$ is the total number of realizations, $T$ is the total simulation time and $\mathbb{I}(k)$ is an indicator function for a collision with the boundary during time step $k$. The diffusion coefficient can be estimated by summing across all faces,

$$\mathbf{D}^* = \mathbf{I} + \frac{1}{\Omega_l} \sum_{i=0}^{N_{fa}} \mathbf{n}\mathbf{b}_i A_i \tag{5.14}$$

where $N_{fa}$ is the total number of faces making up the boundary.

The Laplace equation with pure Neumann boundary conditions has a unique solution up to a constant. In order to set this constant, we will introduce a Dirichlet boundary condition where appropriate. The Dirichlet boundary condition in this probabilistic framework has been previously discussed [79], and is handled by halting the random walk when it intersects with that boundary. Because we are setting this constant to zero, in practice it is an absorbing boundary condition.

A simple example may illuminate the purposed method. Consider a 2D unit box with outward facing normals. In 2D, (5.7) for $b_x$ is

$$-n_x + n_x \frac{\partial b_x}{\partial x} + n_y \frac{\partial b_x}{\partial y} = 0 \tag{5.15}$$

$$\tag{5.16}$$

On the boundaries $x = 0$ or 1, we have $\partial b_x / \partial x = 1$. When a random walk intersects a face belonging to those boundaries, a local count will be incremented. On the boundary $y = 0$ or 1, $\partial b_x / \partial y = 0$, and $b_x$ is therefore an arbitrary constant. We set this constant to 0, which in the probabilistic formulation is an absorbing boundary condition, where the random walk is halted and removed from the simulation.

In the case where neither $(n_x, n_y)$ is zero, a probabilistic representation of the boundary condition is unclear. Inspired by the asymptotic behavior in the unit cube, we propose the following algorithm:

1. Each time step the RBM intersects with a boundary, choose a random variable $p_n \in [0, 1)$
2. If $p_n < n_d$, reflect and increment a local count for that face
3. If $p_n \geq n_d$, remove the particle from the simulation (absorb)

where $d = \{x, y, z\}$ depending on solving for $b = \{b_x, b_y, b_z\}$. In the 2D unit box described above, on the boundaries $x = 0$ or 1, condition 2 will always apply, and the RBM will always reflect on that boundary, as desired. Similarly, when an RBM interesects with a face on $y = 0$ or 1, that RBM will be halted and removed from the simulation. Presently, results using this method have been mixed. We are currently exploring permutations of this method, but the basic idea seems to be on the right track.

### 5.2.2 Preliminary Results

An initial validation can be performed by comparing the proposed probabilistic formulation with classic finite difference methods. Consider the unit cube in 3D. In this case the effective diffusion coefficient is unitary, as there are no diffusive barriers, but we can compare the solution $b(x)$ on the boundary. A comparison of a finite difference solution and the probabilistic solution with different numbers of realizations $N$ is shown in Figure 5.3. These plots show the same quantitative solution, and a plot of the centerline solution in Figure 5.4 shows good agreement. Current efforts are geared toward improving the accuracy of the solution.

## 5.3 Conclusion

We have shown preliminary results of a probabilistic framework for solving the Neumann problem, with a proposed application to determine the effective diffusion coefficient in a computational reconstruction of neural tissue. Although issues remain, the qualitative agreement seen in Figure 5.3 suggests the method is tractable. The remaining task is to determine the source of the error in the solution seen in Figure 5.4, and to determine how to properly account for nonorthogonal

boundary conditions. We believe these problems are surmountable and suggest this method will provide a powerful means of analyzing problems with complex surface meshes in a variety of contexts. A possible alternative application is chemistry within a battery with a complex shape, a problem being addressed by another member of our group.

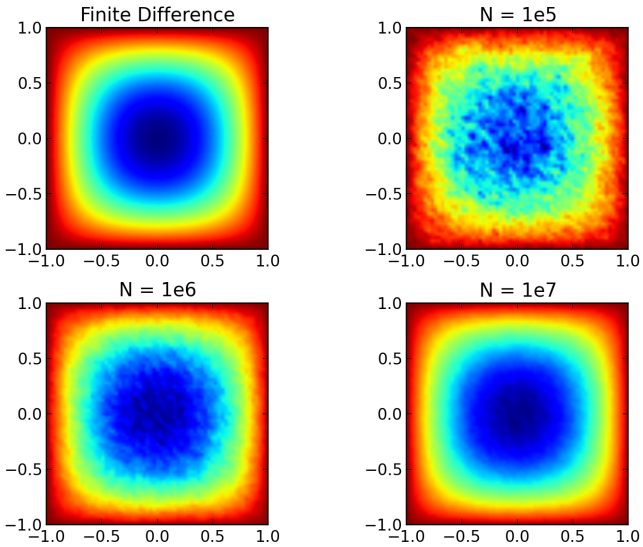


**Figure 5.3**: A comparison of the solution of (5.7) using finite difference (upper left), and the probabilistic framework with $N$ realizations. The solution improves as the number of realizations increases, as expected.

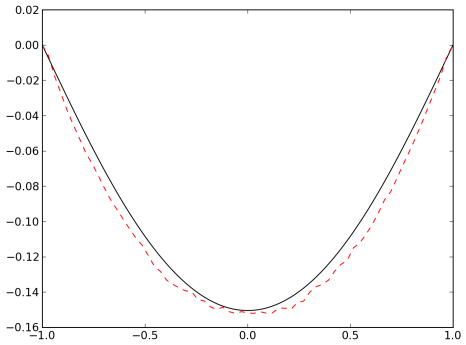


**Figure 5.4**: A comparison of the solutions along the centerline for finite difference (smooth black) and the proposed probabilistic method (broken red). Differences in shape and scale can be seen, indicating errors in the method.

# 6 Conclusions

Biological systems are particularly interesting to study due the fundamental influence of stochasticity. As imaging technology has undergone rapid improvements in spatial and temporal resolution, theoretical models of these systems have become increasingly important for understanding new data. In parallel with efforts in the hydrogeological community, biological multi-scale models are becoming increasingly common, elucidating complex mechanisms that cannot be understood by simple models alone. The connection between molecular dynamics, diffusive dynamics and tissue dynamics is rapidly being bridged as each subfield has begun to have the computational power necessary to push a significant overlap between the scales. The field is reaching a point in which general guiding principles are becoming discernible , and sophisticated engineering of these systems is becoming feasible.

In this work, we investigate a model biological system by tracking single diffusing particles. These trajectories are used to find mathematical tools for both analysis and modeling. Specifically, we found that different stochastic processes may be good models for specific biological transport motifs, e.g. fractional Brownian motion in active cytoskeletal transport and continuous time random walks for free diffusion within the cystsol. We also propose a new scheme for finding the anomalous diffusion coefficient from stochastic trajectories that is particularly suited for discerning nonstationary behavior in single trajectories. Using this method, we show how a broad distribution of scalings can be seen for a given environment.

To probe the effect of crowding, improvements are proposed to a Monte Carlo simulator of diffusion and reaction. Specifically, a method of implementing

hard sphere particle representations and a mean field hydrodynamics approximation is described. We discuss how to handle interactions between particles and surfaces of complex geometries in this framework. A possible application is to investigate how space filling particles effect dynamics in realistic geometries.

Finally, a novel approach for finding the effective diffusion coefficient in a surface mesh is introduced. The method uses Monte Carlo simulations of reflecting Brownian motion to probabilistically calculate the solution to a closure problem. We present preliminary results in a simple geometry showing good agreement to the solution calculated using a finite difference method. Furthermore, we outline a possible way to extend the method to a more complex geometry, which we are currently resolving.

An interesting prospect is how anomalous transport could be used actively in a system to control biochemical pathways. Evidence suggests subdiffusive transport acts to increase reaction rates by increasing the rate of encounter, providing an evolutionary advantage to designs with highly concentrated systems. An intriguing control method is using actively superdiffusive transport, such as that seen on the cytoskeleton, to control rates in a reaction scheme. For example, one could imagine a scheme in which reaction partners are kept separate by the dense intracellular matrix of proteins, organelles and cytoskeletal components, but are brought into the same region when a reaction is needed. In this way, segregation of chemical partners could be accomplished without the use of discrete structures, such as an organelle. There is also evidence that the ability to diffuse freely is strongly effected by the presence of ATP. [137, 101] Cytoskeletal transport in biology uses ATP, and it has been suggested that this relationship between ATP and diffusive motion is evidence that transport not only moves cargo along the cytoskeleton, but may also provide local fluctuations that allow molecules to diffuse more freely. Understanding how these transport motifs interact will be critical in understanding cellular function.

# A Appendix A

## A.1 Microscope Control Details

Initial designs of our microscope used a software solution to communicate with the DDS using the common USB protocol. This allowed simple scanning, but was limiting due to USB packet timing constraints and the inherent asynchrony in USB. To reach the physical limits of our scanner, for this study a custom FPGA firmware is developed to drive the DDS. An FPGA provides an affordable and powerful method to implement a hardware solution, which is excellent for time sensitive tasks where hardware will greatly outperform software. The main problem this avoids is the intrinsic USB inter-packet delays, therefore guaranteeing excellent timing control. Furthermore, limits on USB packets require repeated volume scans to be broken into smaller chunks, which creates obvious problems due to inter-packet delays, but also creates synchronization issues due to limits on the number of sync signals an oscilloscope will recognize in a single acquisition. By ensuring timing is fully controlled by the FPGA, with the only control coming from a single external start signal, greatly improving our scan capabilities given the limitations of the hardware.

Standard operation proceeds as follows. A description of the volume to acquire is sent over USB using a metalanguage in hexadecimal characters, and saved into memory. At that point, either a "Start" signal can be included in the original signal, or the FPGA will stand ready waiting for a new signal, in both cases containing the number of repeats and instructions to begin scanning. At the start of a scan the metalanguage is converted into a series of commands that are delivered to the DDS, which will perform the required series of frequency sweeps to produce

the desired scan pattern. The start signal will also pulse a synchronization to the oscilloscope, triggering the acquisition of the incoming photomultiplier output. Finally, the acquired data is computationally reconstructed into a final stack of images for each time point.

# Bibliography


[1] E. Abbe. Contributions to the theory of the microscope and microscopic detection (translated from german). *Arch Mikroskop Anat*, 9:413–468, 1873.

[2] M. D. Abramoff, P. J. Magalhaes, and S. J. Ram. Image processing with imagej. *Biophotonics Int.*, 11(7):36–42, 2004.

[3] R. Acharya, S. Van der Zee, and A. Leijnse. Transport modeling of nonlinearly adsorbing solutes in physically heterogeneous pore networks. *Water Resour. Res.*, 41(2), 2005.

[4] P. M. Adler. *Porous Media: Geometry and Transports*. Butterworth-Heinemann, 1992.

[5] B. Alberts, A. Johnson, J. Lewis, M. Raff, K. Roberts, and P. Walter. *Molecular Biology of the Cell*. Garland Science, New York, 2008.

[6] T. Ando and J. Skolnick. Crowding and hydrodynamic interactions likely dominate in vivo macromolecular motion. *Proc. Natl. Acad. Sci. U.S.A.*, 107(43):18457–18462, 2010.

[7] J.-L. Auriault and P. Adler. Taylor dispersion in porous media: analysis by multiple scale expansions. *Adv. Water Resour.*, 18(4):217–226, 1995.

[8] D. Axelrod, D. Koppel, J. Schlessinger, E. Elson, and W. Webb. Mobility measurement by analysis of fluorescence photobleaching recovery kinetics. *Biophys. J.*, 16(9):1055–1069, 1976.

[9] D. S. Banks and C. Fradin. Anomalous diffusion of proteins due to molecular crowding. *Biophys. J.*, 89(5):2960–2971, 2005.

[10] E. Barkai, Y. Garini, and R. Metzler. Strange kinetics of single molecules in living cells. *Phys. Today*, 65(8):29–35, 2012.

[11] E. Barkai, R. Metzler, and J. Klafter. From continuous time random walks to the fractional fokker-planck equation. *Phys. Rev. E*, 61(1):132, 2000.

[12] M. Bates, M. Burns, and A. Meller. Dynamics of dna molecules in a membrane channel probed by active control techniques. *Biophys. J.*, 84(4):2366 – 2372, 2003.

[13] I. Battiato. *Hybrid models of transport in crowded environments*. PhD thesis, 2010.

[14] I. Battiato and D. Tartakovsky. Applicability regimes for macroscopic models of reactive transport in porous media. *J. Contam. Hydrol.*, 120:18–26, 2011.

[15] B. Berkowitz, A. Cortis, M. Dentz, and H. Scher. Modeling non-fickian transport in geological formations as a continuous time random walk. *Rev. Geophys.*, 44(2), 06 2006.

[16] B. Berkowitz, A. Cortis, M. Dentz, and H. Scher. Modeling non-Fickian transport in geological formations as a continuous time random walk. *Rev. Geophys.*, 44:RG2003, 2006.

[17] E. Betzig, G. H. Patterson, R. Sougrat, O. W. Lindwasser, S. Olenych, J. S. Bonifacino, M. W. Davidson, J. Lippincott-Schwartz, and H. F. Hess. Imaging intracellular fluorescent proteins at nanometer resolution. *Science*, 313(5793):1642–1645, 2006.

[18] J.-P. Bouchaud and A. Georges. Anomalous diffusion in disordered media: Statistical mechanisms, models and physical applications. *Phys. Rep.*, 195(45):127 – 293, 1990.

[19] D. Brockmann, L. Hufnagel, and T. Geisel. The scaling laws of human travel. *Nature*, 439(7075):462–465, 01 2006.

[20] I. Bronstein, Y. Israel, E. Kepten, S. Mai, Y. Shav-Tal, E. Barkai, and Y. Garini. Transient anomalous diffusion of telomeres in the nucleus of mammalian cells. *Phys. Rev. Lett.*, 103:018102, Jul 2009.

[21] G. Brosamler. A probalistic solution of the neumann problem. *Math. Scand.*, 38:137–147, 1976.

[22] M. Brunstein, L. Bruno, M. Desposito, and V. Levi. Anomalous dynamics of melanosomes driven by myosin-v in xenopus laevis melanophores. *Biophys. J.*, 97(6):1548 – 1557, 2009.

[23] A. Bullen, S. Patel, and P. Saggau. High-speed, random-access fluorescence microscopy: I. high-resolution optical recording with voltage-sensitive dyes and ion indicators. *Biophys. J.*, 73(1):477–491, 1997.

[24] S. Burov, J.-H. Jeon, R. Metzler, and E. Barkai. Single particle tracking in systems showing anomalous diffusion: the role of weak ergodicity breaking. *Phys. Chem. Chem. Phys.*, 13:1800, 2011.

[25] A. Caspi, R. Granek, and M. Elbaum. Enhanced diffusion in active intracellular transport. *Phys. Rev. Lett.*, 85(26):5655–5658, December 2000.

[26] A. Caspi, R. Granek, and M. Elbaum. Diffusion and directed motion in cellular transport. *Phys. Rev. E*, 66(1):011916, Jul 2002.

[27] J.-F. Coeurjolly. *dvfBm: Discrete variations of a fractional Brownian motion*, 2009. R package version 1.0.

[28] J. S. Coggan, T. M. Bartol, E. Esquenazi, J. R. Stiles, S. Lamont, M. E. Martone, D. K. Berg, M. H. Ellisman, and T. J. Sejnowski. Evidence for ectopic neurotransmission at a neuronal synapse. *Science*, 309(5733):446–451, 2005.

[29] J.-A. Conchello and J. W. Lichtman. Optical sectioning microscopy. *Nat. Methods*, 2(12):920–931, 2005.

[30] E. Coumans. Bullet multiphysics engine. accessed 2014-2-28, from http://www.bulletphysics.org.

[31] A. M. Dale and E. Halgren. Spatiotemporal mapping of brain activity by integration of multiple imaging modalities. *Curr. Opin. Neurobiol.*, 11(2):202–208, 2001.

[32] E. Dauty and A. Verkman. Molecular crowding reduces to a similar extent the diffusion of small solutes and macromolecules: measurement by fluorescence correlation spectroscopy. *J. Mol. Recognit.*, 17(5):441–447, 2004.

[33] W. Deng and E. Barkai. Ergodic properties of fractional brownian-langevin motion. *Phys. Rev. E*, 79:011112, Jan 2009.

[34] A. Diaspro, G. Chirico, and M. Collini. Two-photon fluorescence excitation and related techniques in biological microscopy. *Q. Rev. Biophys.*, 38(02):97–166, 2005.

[35] J.-E. Dietrich and T. Hiiragi. Stochastic patterning in the mouse preimplantation embryo. *Development*, 134(23):4219–4231, 2007.

[36] M. Dittrich, J. M. Pattillo, J. D. King, S. Cho, J. R. Stiles, and S. D. Meriney. An excess-calcium-binding-site model predicts neurotransmitter release at the neuromuscular junction. *Biophys. J.*, 104(12):2751–2763, 2013.

[37] J. A. Dix and A. Verkman. Crowding effects on diffusion in solutions and cells. *Ann. Rev. Biophys.*, 37(1):247–263, 2008. PMID: 18573081.

[38] A. Einstein. On the movement of small particles suspended in stationary liquids required by the molecular-kinetic theory of heat. *Annalen der Physik*, 17(549-560):16, 1905.

[39] R. J. Ellis. Macromolecular crowding: an important but neglected aspect of the intracellular environment. *Curr. Opin. Struc. Biol.*, 11(1):114–119, 2001.

[40] D. Ernst, M. Hellmann, J. Kohler, and M. Weiss. Fractional brownian motion in crowded fluids. *Soft Matter*, 8:4886–4889, 2012.

[41] M. I. Freidlin. *Functional Integration and Partial Differential Equations*. Number 109. Princeton university press, 1985.

[42] M. H. Friedman. *Principles and Models of Biological Transport*. Springer, New York, 2008.

[43] C. W. Gardiner. *Handbook of Stochastic Methods*, volume 3. Springer Berlin, 1985.

[44] C. W. Gardiner. *Handbook of Stochastic Methods for Physics, Chemistry and the Natural Sciences*. Springer-Verlag, Berlin; New York, 1990.

[45] M. K. Gardner, B. D. Charlebois, I. M. Jańosi, J. Howard, A. J. Hunt, and D. J. Odde. Rapid microtubule self-assembly kinetics. *Cell*, 146(4):582 – 592, 2011.

[46] I. Golding and E. C. Cox. Physical nature of bacterial cytoplasm. *Phys. Rev. Lett.*, 96:098102, Mar 2006.

[47] B. Grewe, D. Langer, H. Kasper, B. Kampa, and F. Helmchen. High-speed in vivo calcium imaging reveals neuronal network activity with near-millisecond precision. *Nat. Methods*, 7(5):399–405, May 2010.

[48] M. G. Gustafsson. Surpassing the lateral resolution limit by a factor of two using structured illumination microscopy. *J. Microsc.*, 198(2):82–87, 2000.

[49] D. Hall and A. P. Minton. Macromolecular crowding: qualitative and semi-quantitative successes, quantitative challenges. *BBA-Proteins Proteom.*, 1649(2):127–139, 2003.

[50] P. Hänggi. Stochastic resonance in biology how noise can enhance detection of weak signals and help improve biological information processing. *ChemPhysChem*, 3(3):285–290, 2002.

[51] Y. He, S. Burov, R. Metzler, and E. Barkai. Random time-scale invariant diffusion and transport coefficients. *Phys. Rev. Lett.*, 101:058101, Jul 2008.

[52] S. W. Hell and J. Wichmann. Breaking the diffraction resolution limit by stimulated emission: stimulated-emission-depletion fluorescence microscopy. *Opt. Lett.*, 19(11):780–782, 1994.

[53] M. Hetzer, D. Bilbao-Cortes, T. C. Walther, O. J. Gruss, and I. W. Mattaj. Gtp hydrolysis by ran is required for nuclear envelope assembly. *Mol. Cell.*, 5(6):1013–1024, 2000.

[54] D. Heyes. Brownian dynamics simulations of self and collective diffusion of near hard sphere colloidal liquids: inclusion of many-body hydrodynamics. *Mol. Phys.*, 87(2):287–297, 1996.

[55] F. Höfling and T. Franosch. Anomalous transport in the crowded world of biological cells. *Rep. Prog. Phys.*, 76(4):046602, 2013.

[56] J. R. M. Hosking. Modeling persistence in hydrological time series using fractional differencing. *Water Resour. Res.*, 20(12):1898–1908, 1984.

[57] K. Jaqaman, D. Loerke, M. Mettlen, H. Kuwata, S. Grinstein, S. L. Schmid, and G. Danuser. Robust single-particle tracking in live-cell time-lapse sequences. *Nat. Methods*, 5(8):695–702, 2008.

[58] A. Javer, Z. Long, E. Nugent, M. Grisi, K. Siriwatwetchakul, K. D. Dorfman, P. Cicuta, and M. Cosentino Lagomarsino. Short-time movement of e. coli chromosomal loci depends on coordinate and subcellular localization. *Nat. Commun.*, 4, June 2013.

[59] J.-H. Jeon and R. Metzler. Analysis of short subdiffusive time series: scatter of the time-averaged mean-squared displacement. *J. Phys. A-Math Theor.*, 43(25):252001, 2010.

[60] J.-H. Jeon, V. Tejedor, S. Burov, E. Barkai, C. Selhuber-Unkel, K. Berg-Sørensen, L. Oddershede, and R. Metzler. *In Vivo* anomalous diffusion and weak ergodicity breaking of lipid granules. *Phys. Rev. Lett.*, 106:048103, Jan 2011.

[61] E. R. Kandel, J. H. Schwartz, T. M. Jessell, et al. *Principles of Neural Science*, volume 4. McGraw-Hill New York, 2000.

[62] P. J. Keller, A. D. Schmidt, J. Wittbrodt, and E. H. Stelzer. Reconstruction of zebrafish early embryonic development by scanned light sheet microscopy. *Science*, 322(5904):1065–1069, 2008.

[63] E. Kepten, I. Bronshtein, and Y. Garini. Improved estimation of anomalous diffusion exponents in single-particle tracking experiments. *Phys. Rev. E*, 87:052713, May 2013.

[64] R. A. Kerr, T. M. Bartol, B. Kaminsky, M. Dittrich, J.-C. J. Chang, S. B. Baden, T. J. Sejnowski, and J. R. Stiles. Fast monte carlo simulation methods for biological reaction-diffusion systems in solution and on surfaces. *SIAM J. Sci. Comput.*, 30(6):3126–3149, 2008.

[65] J. W. J. Kerssemakers, E. Laura Munteanu, L. Laan, T. L. Noetzel, M. E. Janson, and M. Dogterom. Assembly dynamics of microtubules at molecular resolution. *Nature*, 442(7103):709–712, 08 2006.

[66] S. Khan, T. Reese, N. Rajpoot, and A. Shabbir. Spatiotemporal maps of camkii in dendritic spines. *J. Comput. Neurosci.*, 33:123–139, 2012.

[67] J. P. Kinney, J. Spacek, T. M. Bartol, C. L. Bajaj, K. M. Harris, and T. J. Sejnowski. Extracellular sheets and tunnels modulate glutamate diffusion in hippocampal neuropil. *J. Comp. Neurol.*, 521(2):448–464, 2013.

[68] P. Kirkby, K. Nadella, and A. Silver. A compact acousto-optic lens for 2d and 3d femtosecond based 2-photon microscopy. *Opt. Express*, 18(13):13721–13745, 2010.

[69] M. Klann and H. Koeppl. Spatial simulations in systems biology: from molecules to cells. *Int. J. Mol. Sci.*, 13(6):7798–7827, 2012.

[70] A. Klemm, H.-P. Müller, and R. Kimmich. Nmr microscopy of pore-space backbones in rock, sponge, and sand in comparison with random percolation model objects. *Phys. Rev. E*, 55(4):4413, 1997.

[71] D. L. Koch and J. F. Brady. Anomalous diffusion in heterogeneous porous media. *Phys. Fluids*, 31(5):965–973, 1988.

[72] A. B. Kolomeisky and M. E. Fisher. Molecular motors: A theorist's perspective. *Annu. Rev. Phys. Chem.*, 58(1):675–695, 2007.

[73] M. Köpf, C. Corinth, O. Haferkamp, and T. F. Nonnenmacher. Anomalous diffusion of water in biological tissues. *Biophys. J.*, 70(6):2950–2958, 06 1996.

[74] N. H. Kuiper. Tests concerning random points on a circle. *P. K. Ned. Akad. A. Math.*, 63:38–47, 1960.

[75] A. Kusumi and Y. Sako. Cell surface organization by the membrane skeleton. *Curr. Opin. Cell Biol.*, 8(4):566–574, 1996.

[76] E. Levine and T. Hwa. Stochastic fluctuations in metabolic pathways. *Proc. Natl. Acad. Sci. USA*, 104(22):9224–9229, 2007.

[77] A. Lubelski, I. M. Sokolov, and J. Klafter. Nonergodicity mimics inhomogeneity in single particle tracking. *Phys. Rev. Lett.*, 100:250602, Jun 2008.

[78] K. Luby-Phelps. Cytoarchitecture and physical properties of cytoplasm: volume, viscosity, diffusion, intracellular surface area. *Int. Rev. Cytol.*, 192:189 – 221, 2000.

[79] S. Maire and E. Tanré. Monte carlo approximations of the neumann problem. *Monte Carlo Methods and Applications*, 19(3):201–236, 2013.

[80] B. Mandelbrot and J. Van Ness. Fractional brownian motions, fractional noises and applications. *SIAM Rev.*, 10(4):422–437, 1968.

[81] R. N. Mantegna and H. E. Stanley. Scaling behaviour in the dynamics of an economic index. *Nature*, 376(6535):46–49, 07 1995.

[82] J.-M. Marin, K. Mengersen, and C. P. Robert. Bayesian modelling and inference on mixtures of distributions. In D. Dey and C. R. Rao, editors, *Handbook of Statistics*.

[83] O. Medalia, I. Weber, A. S. Frangakis, D. Nicastro, G. Gerisch, and W. Baumeister. Macromolecular architecture in eukaryotic cells visualized by cryoelectron tomography. *Science*, 298(5596):1209–1213, 2002.

[84] A. Meller. Dynamics of polynucleotide transport through nanometre-scale pores. *J. Phys. Condens. Mat.*, 15(17):R581, 2003.

[85] R. Metzler and J. Klafter. The random walk's guide to anomalous diffusion: a fractional dynamics approach. *Phys. Rep.*, 339(1):1 – 77, 2000.

[86] R. Metzler and J. Klafter. The restaurant at the end of the random walk: recent developments in the description of anomalous transport by fractional dynamics. *J. Phys. A-Math Gen.*, 37(31):R161–R208, 2004.

[87] X. Michalet. Mean square displacement analysis of single-particle trajectories with localization error: Brownian motion in an isotropic medium. *Phys. Rev. E*, 82:041914, Oct 2010.

[88] A. P. Minton. The influence of macromolecular crowding and macromolecular confinement on biochemical reactions in physiological media. *J. Biol. Chem.*, 276(14):10577–10580, 2001.

[89] E. W. Montroll and G. H. Weiss. Random walks on lattices. ii. *J. Math. Phys.*, 6:167–181, 1965.

[90] N. Muramatsu and A. P. Minton. Tracer diffusion of globular proteins in concentrated protein solutions. *Proc. Natl. Acad. Sci. USA*, 85(9):2984–2988, 1988.

[91] D. Murphy and M. Davidson. *Fundamentals of Light Microscopy and Electronic Imaging*. Wiley, 2012.

[92] S. P. Neuman and D. M. Tartakovsky. Perspective on theories of anomalous transport in heterogeneous media. *Adv. Water Resour.*, 32(5):670–680, 2009.

[93] T. Neusius, I. M. Sokolov, and J. C. Smith. Subdiffusion in time-averaged, confined random walks. *Phys. Rev. E*, 80:011109, Jul 2009.

[94] L. C. Nitsche and H. Brenner. Eulerian kinematics of flow through spatially periodic models of porous media. *Arch. Ration. Mech. An.*, 107(3):225–292, 1989.

[95] L. Niu and J. Yu. Investigating intracellular dynamics of ftsz cytoskeleton with photoactivation single-molecule tracking. *Biophys. J.*, 95(4):2009–2016, 2008.

[96] B. Øksendal. *Stochastic differential equations*. Springer, 2003.

[97] E. Özarslan, P. J. Basser, T. M. Shepherd, P. E. Thelwall, B. C. Vemuri, and S. J. Blackband. Observation of anomalous diffusion in excised tissue by characterizing the diffusion-time dependence of the mr signal. *J. Magn. Reson.*, 183(2):315 – 323, 2006.

[98] D. OMalley and J. H. Cushman. Random renormalization group operators applied to stochastic dynamics. *J. Stat. Phys.*, 149(5):943–950, 2012.

[99] D. OMalley and J. H. Cushman. A renormalization group classification of nonstationary and/or infinite second moment diffusive processes. *J. Stat. Phys.*, 146:989–1000, 2012.

[100] D. OMalley and J. H. Cushman. Two-scale renormalization-group classification of diffusive processes. *Phys. Rev. E*, 86(1):011126, 2012.

[101] B. R. Parry, I. V. Surovtsev, M. T. Cabeen, C. S. OHern, E. R. Dufresne, and C. Jacobs-Wagner. The bacterial cytoplasm has glass-like properties and is fluidized by metabolic activity. *Cell*, 156(1):183–194, 2014.

[102] S. R. P. Pavani, M. A. Thompson, J. S. Biteen, S. J. Lord, N. Liu, R. J. Twieg, R. Piestun, and W. Moerner. Three-dimensional, single-molecule fluorescence imaging beyond the diffraction limit by using a double-helix point spread function. *Proc. Natl. Acad. Sci. U.S.A.*, 106(9):2995–2999, 2009.

[103] M. J. Perrin. *Brownian Movement and Molecular Reality: Translated from the Annales de Chimie Et de Physique, 8 Series, September 1909, by F. Soddy*. Taylor & Francis, 1910.

[104] H. Qian, M. Sheetz, and E. Elson. Single particle tracking. analysis of diffusion and flow in two-dimensional systems. *Biophys. J.*, 60(4):910–921, 1991.

[105] S. Ram, E. S. Ward, and R. J. Ober. Beyond rayleigh's criterion: A resolution measure with application to single-molecule microscopy. *Proc. Natl. Acad. Sci. USA*, 103(12):4457–4462, 2006.

[106] B. Regner, D. Vučinić, C. Domnisoru, T. Bartol, M. Hetzer, D. Tartakovsky, and T. Sejnowski. Anomalous diffusion of single particles in cytoplasm. *Biophys. J.*, 104(8):1652 – 1660, 2013.

[107] R. K. Rew, G. P. Davis, S. Emmerson, and H. Davies. Netcdf user's guide for c, an interface for data access, version 3. http://www.unidata.ucar.edu/software/netcdf/ docs/index.html, 1997.

[108] D. Ridgway, G. Broderick, A. Lopez-Campistrous, M. Ruaini, P. Winter, M. Hamilton, P. Boulanger, A. Kovalenko, and M. J. Ellison. Coarse-grained molecular simulation of diffusion and reaction kinetics in a crowded virtual cytoplasm. *Biophys. J.*, 94(10):3748–3759, 2008.

[109] M. J. Rust, M. Bates, and X. Zhuang. Sub-diffraction-limit imaging by stochastic optical reconstruction microscopy (storm). *Nat. Methods*, 3(10):793–796, 2006.

[110] R. Salome, Y. Kremer, S. Dieudonne, J. Leger, O. Krichevsky, C. Wyart, D. Chatenay, and L. Bourdieu. Ultrafast random-access scanning in two-photon microscopy using acousto-optic deflectors. *J. Neurosci. Methods*, 154:161–174, 2006.

[111] G. Samorodnitsky. *Stable Non-Gaussian Random Processes: Stochastic Models with Infinite Variance*. Chapman and Hall/CRC, 1 edition, June 1994.

[112] H. Sanabria, Y. Kubota, and M. N. Waxham. Multiple diffusion mechanisms due to nanostructuring in crowded environments. *Biophys. J.*, 92(1):313–322, 2007.

[113] M. J. Saxton. Anomalous diffusion due to obstacles: a monte carlo study. *Biophys. J.*, 66(2):394–401, 1994.

[114] M. J. Saxton. Wanted: a positive control for anomalous subdiffusion. *Biophys. J.*, 103(12):2411–2422, 2012.

[115] M. J. Saxton and K. Jacobson. Single-particle tracking:applications to membrane dynamics. *Annu. Rev. Bioph. Biom.*, 26(1):373–399, 1997. PMID: 9241424.

[116] H. Scher and M. Lax. Stochastic transport in a disordered solid. i. theory. *Phys. Rev. B*, 7:4491–4502, May 1973.

[117] H. Scher and E. W. Montroll. Anomalous transit-time dispersion in amorphous solids. *Phys. Rev. B*, 12(6):2455, 1975.

[118] A. Scimemi, H. Tian, and J. S. Diamond. Neuronal transporters regulate glutamate clearance, nmda receptor activation, and synaptic plasticity in the hippocampus. *J. Neuro.*, 29(46):14581–14595, 2009.

[119] G. Seisenberger, M. U. Ried, T. Endreß, H. Büning, M. Hallek, and C. Bräuchle. Real-time single-molecule imaging of the infection pathway of an adeno-associated virus. *Science*, 294(5548):1929–1932, 2001.

[120] T. M. Shepherd, E. Özarslan, M. A. King, T. H. Mareci, and S. J. Blackband. Structural insights from high-resolution diffusion tensor imaging and tractography of the isolated rat hippocampus. *Neuroimage*, 32(4):1499–1509, 2006.

[121] B. M. Slepchenko, I. Semenova, I. Zaliapin, and V. Rodionov. Switching of membrane organelles between cytoskeletal transport systems is determined by regulation of the microtubule-based transport. *J. Cell Biol.*, 179(4):635–641, 2007.

[122] S. Song, P. J. Sjöström, M. Reigl, S. Nelson, and D. B. Chklovskii. Highly nonrandom features of synaptic connectivity in local cortical circuits. *PLoS Biol.*, 3(3):e68, 2005.

[123] J. R. Stiles and T. M. Bartol. Monte carlo methods for simulating realistic synaptic microphysiology using mcell. In E. de Schutter, editor, *Computational Neuroscience: Realistic Modeling for Experimentalists*.

[124] J. R. Stiles, D. Van Helden, T. M. Bartol, E. E. Salpeter, and M. M. Salpeter. Miniature endplate current rise times less than 100 microseconds from improved dual recordings can be modeled with passive acetylcholine diffusion from a synaptic vesicle. *Proc. Natl. Acad. Sci. U.S.A.*, 93(12):5747–5752, 1996.

[125] P. Strating. Brownian dynamics simulation of a hard-sphere suspension. *Phys. Rev. E*, 59(2):2175, 1999.

[126] J. Sun and H. Weinstein. Toward realistic modeling of dynamic processes in cell signaling: Quantification of macromolecular crowding effects. *J. Chem. Phys.*, 127(15):155105, 2007.

[127] N. L. Thompson. Fluorescence correlation spectroscopy. In J. R. Lakowicz, editor, *Topics in Fluorescence Spectroscopy*.

[128] I. M. Tolić-Nørrelykke, E.-L. Munteanu, G. Thon, L. Oddershede, and K. Berg-Sørensen. Anomalous diffusion in living yeast cells. *Phys. Rev. Lett.*, 93:078102, Aug 2004.

[129] S. Türkcan, A. Alexandrou, and J.-B. Masson. A bayesian inference scheme to extract diffusivity and potential fields from confined single-molecule trajectories. *Biophys. J.*, 102(10):2288–2298, 5 2012.

[130] G. Urbina-Villalba, M. García-Sucre, and J. Toro-Mendoza. Average hydrodynamic correction for the brownian dynamics calculation of flocculation rates in concentrated dispersions. *Phys. Rev. E*, 68(6):061408, 2003.

[131] R. D. Vale. The molecular motor toolbox for intracellular transport. *Cell*, 112(4):467 – 480, 2003.

[132] A. S. Verkman. Solute and macromolecule diffusion in cellular aqueous compartments. *Trends Biochem. Sci.*, 27(1):27 – 33, 2002.

[133] G. M. Viswanathan, V. Afanasyev, S. V. Buldyrev, E. J. Murphy, P. A. Prince, and H. E. Stanley. Levy flight search patterns of wandering albatrosses. *Nature*, 381(6581):413–415, 05 1996.

[134] M. Von Smoluchowski. Zur kinetischen theorie der brownschen molekularbewegung und der suspensionen. *Annalen der Physik*, 326(14):756–780, 1906.

[135] D. Vučinić and T. J. Sejnowski. A compact multiphoton 3d imaging system for recording fast neuronal activity. *PLoS ONE*, 2(8):e699, 2007.

[136] D. Wang, L. She, Y.-n. Sui, X.-b. Yuan, Y. Wen, and M.-m. Poo. Forward transport of proteins in the plasma membrane of migrating cerebellar granule cells. *Proc. Natl. Acad. Sci. U.S.A.*, 109(51):E3558–E3567, 2012.

[137] S. C. Weber, A. J. Spakowitz, and J. A. Theriot. Nonthermal atp-dependent fluctuations contribute to the in vivo motion of chromosomal loci. *Proc. Natl. Acad. Sci. U.S.A.*, 109(19):7338–7343, 2012.

[138] S. Whitaker. *The Method of Volume Averaging*, volume 13. Springer, 1999.

[139] D. Williams and C. Carter. *Transmission Electron Microscopy: A Textbook for Materials Science*. Cambridge library collection. Springer, 2009.

[140] A. T. Wood and G. Chan. Simulation of stationary gaussian processes in [0, 1] d. *J. Comput. Graph. Stat.*, 3(4):409–432, 1994.

[141] H.-X. Zhou, G. Rivas, and A. P. Minton. Macromolecular crowding and confinement: biochemical, biophysical, and potential physiological consequences. *Ann. Rev. Biophys.*, 37:375, 2008.